Stabilisation of Hydrodynamic Instabilities by Critical Layers in Acoustic Lining Boundary Layers[*]

Matthew J. King[†] and Edward J. Brambley[‡]
Mathematics Institute, University of Warwick, Coventry CV4 7AL, UK
WMG, University of Warwick, Coventry CV4 7AL, UK

Acoustics are considered in a straight cylindrical lined duct with an axial mean flow that is uniform apart from a boundary layer near the wall. Within the boundary layer, which may or may not be thin, the flow profile is quadratic and satisfies no-slip at the wall. Time-harmonic modal solutions to the linearised Euler equations are found by solving the Pridmore-Brown equation using Frobenius series. The Briggs–Bers criterion is used to ascertain the spatial stability of the modes, without considering absolute instabilities. The modes usually identified as Hydrodynamic Instabilities are found to interact with the critical layer branch cut, also known as the continuous spectrum. By varying the boundary layer thickness, flow speed, frequency and wall impedance, it is found that these spatial instabilities can be stabilised behind the critical layer branch cut. In particular, spatial instabilities are only found for a boundary layer thinner than a critical boundary layer thickness h_c. The behaviours observed for the uniform-quadratic sheared flow considered here are further compared to a uniform-linear sheared flow, and a uniform slipping flow under the Ingard–Myers boundary condition, where this process of stabilisation is not observed. It is therefore argued that modelling a sufficiently smooth mean flow boundary layer is necessary to predict the correct stability of flow over a lined wall.

I. Introduction

Aircraft noise, and particularly aeroengine noise, has, over recent years, been subjected to ever stricter limitations. Aircraft manufacturers are increasingly relying on numerical simulations to optimize new aircraft designs, and noise limits form a significant constraint on the optimal design. For this reason, acoustic linings are universally used throughout aeroengines in order to reduce particularly unwanted tonal noise. The design and optimization of such linings is therefore of considerable interest, but similarly instability of flow over such linings that could reduce aeroengine efficiency or increase noise are also of interest.

Acoustic linings are typically modelled as an impedance boundary condition at a duct wall. An oscillating pressure $p = p_0 + \text{Re}(\hat{p} \exp\{i\omega t\})$ at the duct wall gives rise to an oscillating flow at the duct wall with normal velocity $v = \text{Re}(\hat{v} \exp\{i\omega t\})$, and the wall impedance is given by $Z = \hat{p}/\hat{v}$. In general, Z is complex and varies with the frequency ω. For an actual aeroengine single-degree-of-freedom perforated-sheet liner, a model for $Z(\omega)$ depending on the various physical parameters was given by Guess [2]. Due to its complexity, a simpler model often used is the mass–spring–damper model [3, 4], also known as the three-parameter model [5], and indeed Tam and Auriault [5] explain how this three-parameter model can be used to efficiently model a liner near particular frequencies in time-domain simulations. There are constraints on the allowable forms of $Z(\omega)$, however, as it must be consistent with a causal time-domain model [6], and Rienstra [6] showed that many empirical models, including the model of Guess [2], do not satisfy these constraints. Taking $Z(\omega)$ to be a constant independent of ω also violates these constraints unless Z is purely real. Rienstra [6] showed the mass–spring–damper model does satisfy these constraints, and then went on to proposed an Extended Helmholtz Resonator model, similar in form to the model of Guess [2], that also satisfies these constraints. Here, we will be concerned with time-harmonic modes with a single frequency ω, and so it might appear that only $Z(\omega)$ for one frequency is needed. However, the form of $Z(\omega)$ affects the stability analysis, and so it is important for stability analyses to use a model corresponding to a causal time-domain model. For this reason, here we will use the mass–spring–damper model, as it is the simplest impedance model that satisfies Rienstra's constraints [6].

It is well known that a mean flow that does not satisfy no-slip at the wall, such as a uniform flow, complicates the impedance boundary condition. The often-used Ingard–Myers [7] boundary condition is illposed in the time domain [8], leading to both numerical and theoretical difficulties, and does not match well with experimental observations [e.g. 9]. It may be regularized by allowing for a thin boundary layer over the wall [10]; while this regularized boundary condition also leads to a significant increase in accuracy when solving the linearized Euler equations [11], it too does not accurately reproduce experimental observations [12]. Various attempts have been made at improved impedance boundary conditions [e.g. 13–15], but to date no impedance boundary condition matches well with experimental observations [16, 17]. An alternative is to include a varying mean flow which satisfies the no-slip condition at the duct wall. This, however, introduces its own complications, including the critical layer, otherwise known as the continuous spectrum [18].

Most investigations of the interaction of sound and acoustic linings consider duct modes in the frequency domain. When considering a non-uniform mean flow in the frequency-domain, the pressure perturbation is governed by the Pridmore-Brown equation [19]. Duct modes are found by solving the Pridmore-Brown equation subject to the impedance boundary condition at the duct wall. A reasonably general solution is then given as a linear sum of these duct modes, with amplitudes fitted to emulate a particular sound source. This is the basis of techniques such as mode-matching [e.g. 20, 21]. Modes also occur as poles in complex analytic methods, such as the the Weiner-Hopf technique [e.g. 22–24]. However, since the Pridmore-Brown equation is not self-adjoint, the duct modes are not necessarily complete, and so a general solution cannot necessarily be described as just a sum of duct modes. This difficulty manifests itself as the critical layer. Solving analytically for the sound generated by a point mass source in a duct, the solution is found to consist not only of a sum of modes, but also includes a Fourier inversion integral around the critical layer [18, 25]. This results in an extra term in the solution downstream of the point mass source, including a neutrally stable non-decaying term if the source is located within the boundary layer [18, 25, 26]. Despite this, the critical layer is often ignored in practice, either explicitly or implicitly, with its contribution argued to be small compared to that of the sum of duct modes, with some justification [18].

One complication of considering duct modes in the frequency domain is determining their direction of propagation; this can be achieved using the Briggs–Bers criterion [27, 28]. Most modes are stable and decay in their direction of propagation, but a number of surface wave modes exist with interesting properties [4, 29], and one such surface wave mode has been labelled a hydrodynamic instability [4]. The hydrodynamic instability is so called because it only exists with a mean flow and has no counterpart without flow [4]. It has been shown to be a convective instability growing spatially in the downstream direction using the Briggs–Bers criterion in both the 2D incompressible case [30] and the 3D compressible case in a cylindrical duct [10]. There is also some experimental [e.g. 31, 32] and numerical [e.g. 33, 34] evidence of spatial instabilities, although the hydrodynamic instability is in most cases the least well theoretically-predicted duct mode; this is in part due to deficiencies in the modelling [e.g. 17, 35], and in part due to the particular sensitivity of the hydrodynamic instability to parameters such as boundary layer thickness (as will be seen here). Because of this, and because of the inconvenience of dealing with an instability in numerical simulations, numerical techniques have been developed [e.g. 36–38] which modify the governing Euler equations to avoid triggering the instability, although care must be taken not to also modify the true acoustical behaviour [34, 39].

Another complication of a frequency-domain analysis is that the frequency of interest must be specified a priori. However, the Briggs–Bers stability analysis shows that, for some convectively unstable systems, the system can choose its own preferred frequency rather than the one prescribed. This is termed absolute instability, and (unlike spatial instabilities) causes the system to grow exponentially in time at the system's preferred frequency. If the system is not absolutely unstable, then the frequency-domain assumption of a single frequency is valid, and the system remains bounded in time. In this case, any instabilities will grow in space but not in time, and are termed spatial, or convective, instabilities; the hydrodynamic instability mentioned above is one such convective instability. Knowledge about absolute instability can also be inferred from knowledge about spatial instabilities: if the system is convectively stable at all frequencies, then absolute instabilities cannot occur. Flow over an acoustic lining is likely to be absolutely unstable for sufficiently thin boundary layers, with the critical boundary layer thickness leading to absolute instability being found in both the 2D incompressible case [30] and the 3D compressible case in a cylindrical duct [10]. When the system is not absolutely unstable, the single-frequency assumption is valid, and the overall stability of the system depends on whether or not the hydrodynamic instability is present, which is the topic of investigation here.

Interestingly, the hydrodynamic instability has been observed [29] in some cases to move behind the critical layer branch cut. This then results in a stable situation, but one for which the critical layer contribution might be the dominant contribution far downstream of the source. However, this has not been investigated further due to the numerical method being unable to track the hydrodynamically unstable surface wave mode behind the critical layer. The Frobenius

method [18] is capable of tracking the mode behind the branch cut, but, for the linear boundary layer flow profile used in that case, the hydrodynamic instability mode never went behind the branch cut. More recently, the Frobenius method has been used to analyse a quadratic boundary layer profile [25], as will also be considered here, and the hydrodynamic instability was found to move behind the critical layer branch cut. Hence, not only was the solution then stable, but the contribution of this hidden mode was included in the Fourier inversion integral around the critical layer, meaning that this mode could still exhibit cut-on behaviour and the non-modal critical layer branch cut may be dominant in the far-field, particularly for a sound source close to the wall; in this case, ignoring the critical layer would give inaccurate results.

In this work, we will examine the stabilization of the hydrodynamic instability as it interacts with and moves behind the critical layer branch cut. In particular, we will observe the effects on this behaviour of boundary layer thickness, Mach number, frequency and impedance. In section II we summarise the Frobenius solutions from King et al. [25] and make use of the code provided. A parameter study is performed in section III. This allows us to find the critical boundary layer thickness that leads to the stabilization of the hydrodynamic 'instability' and comparisons are made to the uniform-linear shear flow of [18] and a uniform flow under the Ingard-Myers boundary condition.

II. Formulation and Solutions to the Pridmore-Brown Equation

The governing equations for what follows are the Euler equations in cylindrical coordinates for an isentropic flow,

$$\frac{\partial \rho}{\partial t} + \frac{\partial (\rho u_x)}{\partial x} + \frac{1}{r}\frac{\partial (r\rho u_r)}{\partial r} + \frac{1}{r}\frac{\partial (\rho u_\theta)}{\partial \theta} = 0, \qquad \frac{Dp}{Dt} = c^2 \frac{D\rho}{Dt},$$

$$\rho\frac{Du_x}{Dt} = -\frac{\partial p}{\partial x}, \qquad \rho\frac{Du_r}{Dt} - \frac{1}{r}\rho u_\theta^2 = -\frac{\partial p}{\partial r}, \qquad \rho\frac{Du_\theta}{Dt} + \frac{1}{r}\rho u_r u_\theta = -\frac{1}{r}\frac{\partial p}{\partial \theta}, \tag{1}$$

where $D/Dt = \partial/\partial t + u_x \partial/\partial x + u_r \partial/\partial r + u_\theta/r \partial/\partial \theta$. We write each variable as a steady mean flow plus a small time-harmonic perturbation of order ϵ and frequency ω,

$$\rho = \rho_0(r) + \text{Re}\big(\epsilon\hat{\rho}e^{i\omega t}\big) + O(\epsilon^2), \qquad p = p_0 + \text{Re}\big(\epsilon\hat{p}e^{i\omega t}\big) + O(\epsilon^2),$$

$$\boldsymbol{u} = (u_x, u_r, u_\theta) = U(r)\boldsymbol{e_x} + \text{Re}\big(\epsilon(\hat{u}, \hat{v}, \hat{w})e^{i\omega t}\big) + O(\epsilon^2), \qquad c^2 = c_0^2(r) + O(\epsilon), \tag{2}$$

where p_0 is necessarily a constant in order that the steady state should satisfy the Euler equations, $U(r)$ is an arbitrary sufficiently-smooth axial velocity profile, and c_0 is the speed of sound for the base flow. While we do not assume a particular equation of state here, for a perfect gas with ratio of specific heats $\gamma = c_p/c_v$ we would have $c_0^2 = \gamma p_0/\rho_0$. All perturbations are then expanded using a Fourier series in θ and a Fourier transform in x. As a result, the pressure perturbation is given as

$$\hat{p}(x, r, \theta) = \frac{1}{2\pi} \sum_{m=-\infty}^{\infty} e^{-im\theta} \int_{-\infty}^{\infty} \widetilde{p}(r; k, m, \omega)e^{-ikx}\,dk, \tag{3}$$

and similarly for the density $\hat{\rho}$ and the velocity components $\hat{u}$, $\hat{v}$ and $\hat{w}$. An important technicality of (3) is that the correct choice of integral contour must be chosen to ensure causality; this is done here using the Briggs–Bers criterion, as described in §III. Ignoring terms of order $O(\epsilon^2)$, which allows us to only consider c^2 to leading order, and solving the Euler equations (1) for the pressure perturbation gives

$$\widetilde{p}'' + \left(\frac{2kU'}{\omega - U(r)k} + \frac{1}{r} - \frac{\rho_0'}{\rho_0}\right)\widetilde{p}' + \left(\frac{(\omega - U(r)k)^2}{c_0^2} - k^2 - \frac{m^2}{r^2}\right)\widetilde{p} = 0 \tag{4a}$$

$$\text{with} \qquad \tilde{v} = \frac{i\widetilde{p}'}{\rho_0(\omega - Uk)}, \tag{4b}$$

where a prime denotes the derivative with respect to r. Equation (4a) is the Pridmore-Brown equation [19].

Here, for simplicity, we assume a constant mean density $\rho_0(r) = \rho_0$, meaning that the flow is homentropic, and resulting in a constant speed of sound $c_0(r) = c_0$. We also, again for simplicity, choose a flow profile $U(r)$ that is uniform except within a boundary layer of width h near the duct wall at $r = a$, where the flow varies quadratically:

$$U(r) = \begin{cases} c_0 M & 0 \le r \le a - h \\ c_0 M(1 - (1 - \frac{a-r}{h})^2) & a - h \le r \le a \end{cases}. \tag{5}$$

3
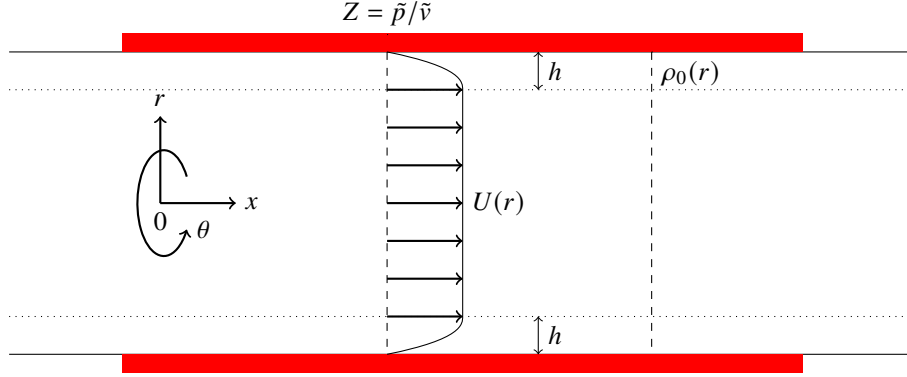
Fig. 1 Schematic of a cylindrical duct with lined walls containing sheared axial flow. $\rho_0(r)$ **is the mean flow density (here taken constant), and** $U(r)$ **is the mean flow velocity, here taken to be uniform outside a boundary layer of width** h. Z **is the boundary impedance and defines the boundary condition at the wall of the duct.**

Here M is the centreline Mach number. This flow profile is not intended to be realistic, but rather sufficiently simple that the critical layer can be investigated explicitly; in practice, other flow profiles are a better approximation to flow boundary layers, although away from the boundary layers a quadratic flow profile shows a reasonable fit to experiments [e.g. 9, §II.B]. Note that we do not need to assume that the boundary layer is thin, so h/a need not be small, unlike some asymptotic analyses [e.g. 10, 13]. This situation is represented schematically in figure 1.

We non-dimensionalize speeds by the sound speed c_0, densities by ρ_0, and distances by the duct radius a. Under these assumptions and non-dimensionalizations, the Pridmore-Brown equation (4a) reduces to

$$\widetilde{p}'' + \left(\frac{2kU'}{\omega - U(r)k} + \frac{1}{r} \right) \widetilde{p}' + \left((\omega - U(r)k)^2 - k^2 - \frac{m^2}{r^2} \right) \widetilde{p} = 0. \tag{6}$$

with

$$U(r) = \begin{cases} M & 0 \leq r \leq 1 - h \\ M(1 - (1 - \frac{1-r}{h})^2) & 1 - h \leq r \leq 1 \end{cases}. \tag{7}$$

We require the solution to be regular at the centreline $r = 0$, and to satisfy an impedance boundary condition at the duct wall $r = 1$. Since our mean flow is nonslipping, $U(1) = 0$, this is given by

$$\widetilde{p}(1) = Z(\omega)\tilde{v}(1), \qquad \text{or equivalently} \qquad \widetilde{p}'(1) - \frac{\mathrm{i}\omega}{Z}\widetilde{p}(1) = 0, \tag{8}$$

where $Z(\omega)$ is the impedance of the duct wall, and a hard wall corresponds to $Z \to \infty$.

In Ref. 25, the Pridmore-Brown equation with this constant-then-quadratic flow profile is solved using a Frobenius method. These solutions are then used to construct a Greens function solution for the inhomogeneous Pridmore-Brown equation, and the Fourier inversion is found. This was used to explore the non-modal contribution of the critical layer. Here, we will use the same Frobenius solutions to find the modes of (6). The important features of the solutions from [25] used here are now briefly summarised.

II.A. Frobenius Solution to the Pridmore-Brown Equation

The Pridmore-Brown equation (6) can be split into two cases according to if we are within the uniform or sheared flow regions (7). When $r < 1 - h$, we are in the uniform flow region, and

$$\widetilde{p}'' + \frac{1}{r}\widetilde{p}' + \left((\omega - Mk)^2 - k^2 - \frac{m^2}{r^2} \right) \widetilde{p} = 0, \tag{9}$$

with solutions in terms of Bessel function of order m. Requiring regularity at $r = 0$, this gives the solution in the uniform flow region as

$$\widetilde{p}(r) = J_m(\alpha r) \qquad \text{with} \qquad \alpha^2 = (\omega - Mk)^2 - k^2. \tag{10}$$

4

In contrast, when $r > 1 - h$, we are in the sheared flow region, and, for this quadratic flow profile, the Pridmore-Brown equation (6) can be written as

$$\widetilde{p}'' + \left(\frac{1}{r} - \frac{2}{r - r_c^-} - \frac{2}{r - r_c^+} \right) \widetilde{p}' + \left(\frac{M^2 k^2}{h^4} (r - r_c^+)^2 (r - r_c^-)^2 - k^2 - \frac{m^2}{r^2} \right) \widetilde{p} = 0, \tag{11}$$

where $r_c^\pm$ are the locations of the critical layer, given by $\omega - U(r_c)k = 0$; note that, in general, r_c will be complex when k or ω are complex. Since $U(r)$ is quadratic for $r > 1 - h$, this is a quadratic equation to solve, with two solutions,

$$r_c^\pm = 1 - h \pm h \sqrt{1 - \frac{\omega}{Mk}}. \tag{12}$$

We choose $\mathrm{Re}(\sqrt{\cdots}) \geq 0$, so that $\mathrm{Re}(r_c^+) \geq 1 - h$; it turns out that r_c^+ is the root we will be most interested in throughout. As in [25], equation (11) can be solved using Frobenius series expansion about r_c^+, resulting in two linearly independent solutions

$$\widetilde{p}_1(r) = \sum_{n=0}^{\infty} a_n (r - r_c^+)^{n+3}, \qquad \widetilde{p}_2(r) = A \widetilde{p}_1(r) \log(r - r_c^+) + \sum_{n=0}^{\infty} b_n (r - r_c^+)^n, \tag{13a}$$

$$\text{where } a_0 = b_0 = 1 \qquad \text{and} \quad A = -\frac{1}{3} \left(\frac{1}{r_c^+ - 1 + h} - \frac{1}{r_c^+} \right) \left(k^2 + \left(\frac{m}{r_c^+} \right)^2 \right) - \frac{2m^2}{3 r_c^{+3}}, \tag{13b}$$

and the a_n and b_n coefficients are given by a recurrence relation in [25]. While the specifics of these solutions are omitted here, we comment that matlab code is provided in [25] to compute these solutions.

To solve the Pridmore-Brown equation across the whole of $r \in [0, 1]$, the two types of solutions above are spliced together such that the resulting solution and its derivative are continuous at $r = 1 - h$:

$$\widetilde{p}(r) = \begin{cases} J_m(\alpha r) & 0 \leq r \leq 1 - h \\ C_1 \widetilde{p}_1(r) + C_2 \widetilde{p}_2(r) & 1 - h \leq r \leq 1, \end{cases} \tag{14}$$

with C_1 and C_2 chosen to ensure continuity of $\widetilde{p}$ and $\widetilde{p}'$ at $r = 1 - h$.

In general, while $\widetilde{p}(r)$ has been constructed to satisfy the regularity boundary condition at $r = 0$ (through the use of the regular Bessel solution $J_m(\alpha r)$ and the exclusion of the singular Bessel solution $Y_m(\alpha r)$), it does not satisfy the impedance boundary condition (8) at $r = 1$. We therefore search for modal solutions by varying k such that $\widetilde{p}(r)$ does satisfy the impedance boundary condition (8) at $r = 1$. This is performed using the matlab code from [25], which uses a variant of the Secant method, and has been verified against finite-difference solutions to the Pridmore-Brown equation. The major advantage of using this method over finite difference is its treatment of the critical layer branch cut.

## II.B. The Critical Layer Branch Cut

The most important detail of the solution method used here is the presence of the log term in (13). The branch of log should clearly be chosen to maintain a continuous solution for $\widetilde{p}_2(r)$, and hence $\widetilde{p}(r)$, along $r \in [1 - h, 1]$. Here, we therefore choose

$$\log(r - r_c^+) = \begin{cases} \log_P \left(\ \mathrm{i}(r - r_c^+) \right) - \pi/2 & \mathrm{Im}(r_c^+) > 0 \\ \log_P \left(-\mathrm{i}(r - r_c^+) \right) + \pi/2 & \mathrm{Im}(r_c^+) < 0 \end{cases}, \tag{15a}$$

$$\text{where} \qquad \log_P(z) = \log(|z|) + \mathrm{i} \arg_P(z) \qquad \text{with} \qquad -\pi < \arg_P(z) \leq \pi, \tag{15b}$$

with $\log_P(z)$ representing the principal branch of log, which is usually the branch computed by numerical implementations of log. The direction of the resulting branch cuts is illustrated in figure 2. The only difficulty is when $\mathrm{Im}(r_c^+) = 0$, and indeed $\mathrm{Im}(r_c^+) \to 0$ from below or from above gives different solutions. We therefore exclude values of k for which $\mathrm{Im}(r_c^+) = 0$ and $\mathrm{Re}(r_c^+) \in [1 - h, 1]$. This results in a branch cut in the complex k plane along the real half line $[\frac{\omega}{M}, \infty)$. We refer to the branch cut in the complex k plane as the critical layer branch cut; this range is also sometimes referred to as the continuous spectrum.

One of the major advantages of the Frobenius method used here is that we are free to choose the branch of log, and so we may in effect analytically continue behind the critical layer branch cut. This is achieved by continuing

5
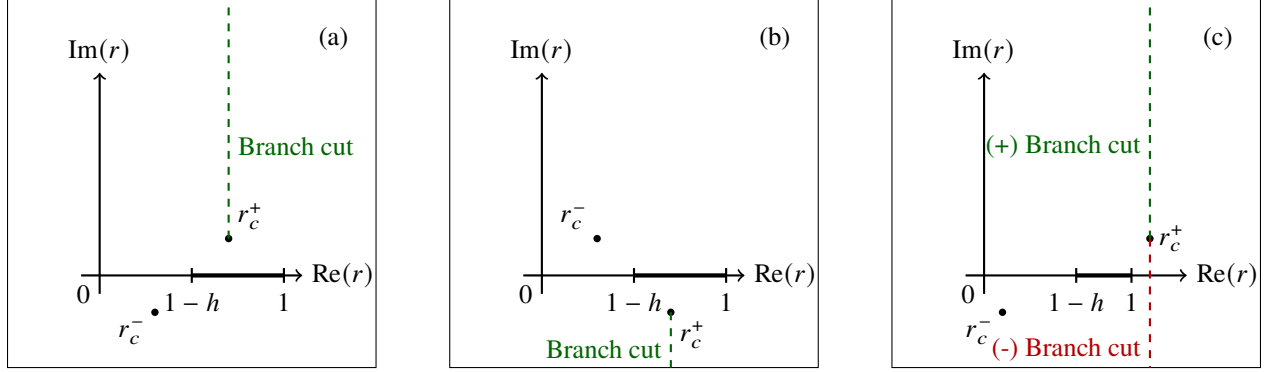
Fig. 2 Schematic of possible locations of the r_c^+ branch cut in the complex r-plane. **(a) A possible choice of branch cut when** $\text{Im}(r_c^+) > 0$ **and** $\text{Re}(r_c^+) < 1$. **(b) Branch cut choice when** $\text{Im}(r_c^+) < 0$ **and** $\text{Re}(r_c^+) < 1$. **(c) When** $\text{Re}(r_c^+) > 1$, **either branch cut may be chosen.**

Table 1 **Parameter Set Values.** A_1, A_2, B_1, B_2, C_1 **and** C_2, **with the subscripts denoting the variation of a single parameter. The Impedance is given by the Mass Spring Damper model,** $Z(\omega) = R + \text{i}(\mu\omega - \frac{K}{\omega})$.

		A	B	C
Frequency	ω	$5_{(1)} \mid 31_{(2)}$	10	10
Centre line Mach Number	M	0.5	0.4	$0.3_{(1)} \mid 0.7_{(2)}$
Azimuthal order	m	0	24	24
Boundary layer thickness	h	0.02	$0.001_{(1)} \mid 0.0075_{(2)}$	0.005
Impedance Mass	μ	0.15	0.08	0.06
Impedance Spring	K	1.15	6	3
Impedance Damper	R	3	1.6	0.75
Impedance	$Z(\omega)$	$3 + 0.52\text{i}_{(1)} \mid 3 + 4.61\text{i}_{(2)}$	$1.6 + 0.2\text{i}$	$0.75 + 0.3\text{i}$

to use one definition of log in (15a), rather than switching between definitions as r_c^+ crosses $[1 - h, 1]$; for example, defining $\log(r - r_c^+) = \log_P(\text{i}(r - r_c^+)) - \pi/2$ gives the correct solution $\widetilde{p}(r)$ when $\text{Im}(k) > 0$, and gives the analytic continuation of that solution behind the branch cut for $\text{Im}(k) < 0$. In so doing, we are able to find any modes that are hidden behind the branch cut. This has two important uses. The first is that modes behind the critical layer branch cut do still contribute to the pressure perturbation $\hat{p}(x, r, \theta)$, though they do so as a Fourier inversion integral around the critical layer branch cut, rather than as an individual mode in its own right; see Ref. 25 for details. Secondly, modes behind the critical layer branch cut can move across the branch cut and become legitimate modes in the usual sense as parameters are varied, and we will see later that, as the boundary layer thickness h is reduced, a mode emerges from the critical layer branch cut and becomes a hydrodynamic instability.

III. Parameter Studies of the Hydrodynamic 'Instability'

In this section, we will be interested in the values of k in the complex k plane for which modal solutions exist for a given frequency ω; such values of $k(\omega)$ are found numerically, as described above. According to the Briggs–Bers criterion [27, 28], a particular mode $k(\omega)$ is stable if $\text{Im}(k(\omega))$ has the same sign as $\text{Im}(k(\omega - \text{i}y))$ as $y \to \infty$, and is convectively unstable otherwise. Here, as in [25], this criterion is used to label modes as stable or unstable by numerically varying the imaginary part of the frequency. This classification ignores the possibility of absolute instabilities, as we are only concerned here with the behaviour of the modal solutions for given values of the frequency ω, and absolute instabilities occur at their own chosen instability frequency.

Throughout the following sections we will use the parameter sets given in table 1. These parameters have been chosen deliberately to demonstrate a variety of behaviours. In particular, while the impedances Z given in table 1
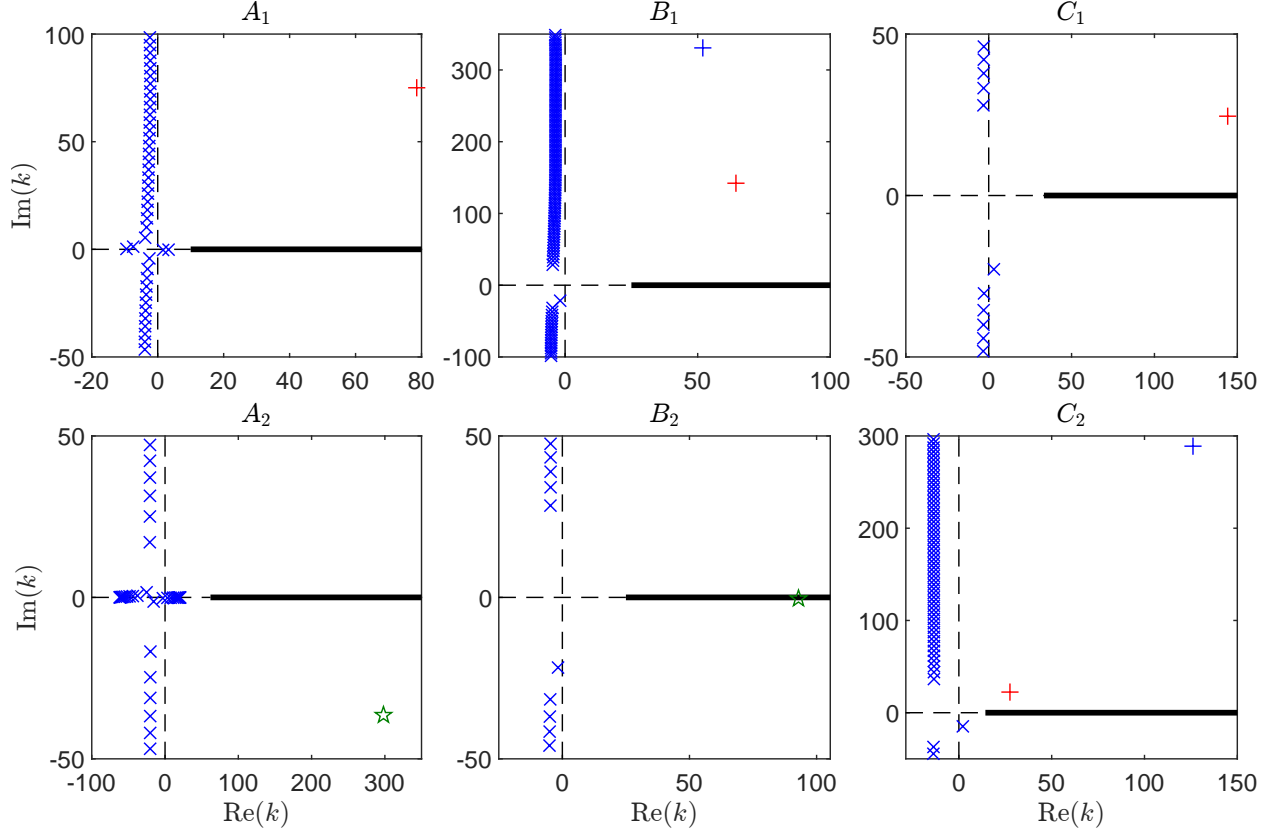
Fig. 3 Locations in the complex k plane of modal solutions for each of the parameter sets listed in table 1. Stable modes are indicated in blue. Unstable modes are coloured red. The hydrodynamic instability mode is marked with a plus (+), while all other modes are marked with a (×). The critical layer branch cut is indicated with by the thick black line. The green star denotes the k_{HI} mode hidden behind the critical layer branch cut.

are typical of impedances seen for acoustic linings used in aeroengines, the mass–spring–damper model is used for simplicity, and is not intended to be an accurate representation of a perforated-plate honeycomb liner. For each of these parameter sets, the locations of the modes in the complex k-plane is shown in figure 3, together with an indication of which modes are stable or unstable. Note that the location of the modes in the complex k-plane in figure 3 depends only on the impedance Z, and not on the individual parameters μ and K in the mass–spring–damper model used to calculate that impedance, although the mass–spring–damper model is necessary for the stability analysis. Throughout this section, we will refer to the potential hydrodynamic instability mode as k_{HI}, whether or not it is actually unstable. This stability may come from either being stabilised by the critical layer, or a change in stability in conjunction with another k_{HI} mode.

In section III.A we will investigate how the hydrodynamic instability is stabilised by the boundary layer thickness h, drawing attention to the threshold value h_c that leads to neutral stability. Following this, in III.B we will vary each of the other parameters and observe how the stability depends on each of these parameters. Finally in III.C we compare the behaviour seen here as the parameters are varied to that seen for a linear boundary layer flow profile, and to that of a uniform flow under the Ingard-Myers boundary condition.

III.A. The effect of boundary layer thickness.

Figure 3 shows a hydrodynamic instability in the upper-right k-plane for parameter set B_1, but not for parameter set B_2. As the only difference between B_1 and B_2 is the boundary layer thickness, this illustrates that increasing the boundary layer thickness can stabilize the hydrodynamic instability. Figure 4 tracks how the modal solutions move in the k-plane as the boundary layer thickness h is varied. From figure 4(B), it can be confirmed that the hydrodynamic instability in B_1 stabilizes by crossing the critical layer branch cut as h is increased. By using the Frobenius method to find modes, we are here able to continue tracking the mode behind the critical layer branch cut as h continues to increase.
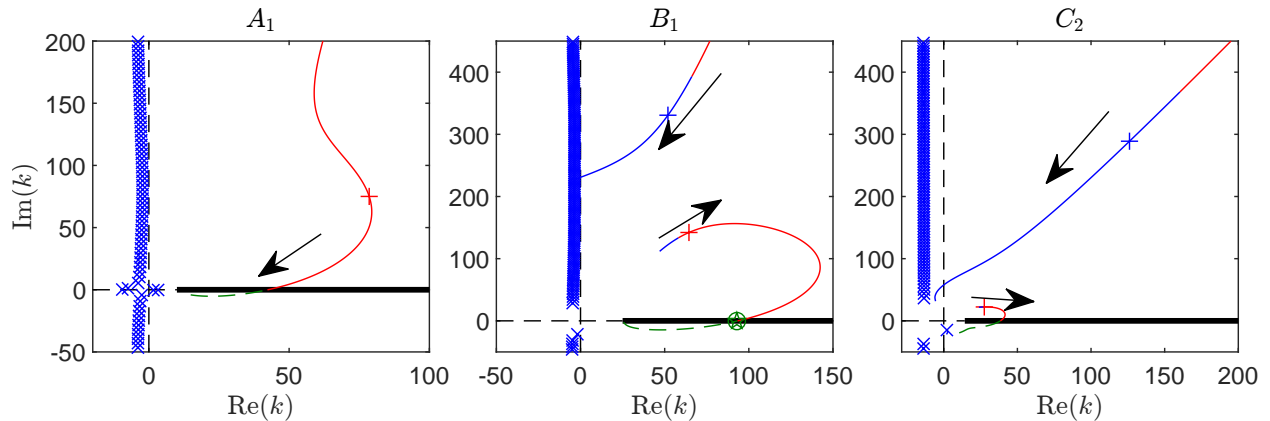
Fig. 4 **Location in the complex k plane of modal solutions, and their trajectories as the boundary layer thickness is varied, for the parameter sets A_1, B_1 and C_2 listed in table 1. The boundary layer thickness h ranges from 5×10^{-4} to 0.1 in the direction of the arrows. The hydrodynamic instability mode for parameter set B_2 has also been included and is circled. Dashed lines denote trajectories hidden behind the critical layer branch cut.**

A similar situation is shown for each case in figure 4; in each case, increasing the boundary layer thickness leads to stability. Moreover, as $h \to 1$, the k_{HI} mode approaches the branch point located at $k = \omega/M$ from behind the branch cut. This appears to be true independent of the impedance, frequency, and flow speed, suggesting that the purely parabolic Poiseuille flow corresponding to $h = 1$ does not exhibit a hydrodynamic instability in any case.

### III.A.1. Changes in stability when varying the boundary layer thickness

In cases B and C_2 in figure 4, it can additionally be observed that for some value of h the unstable behaviour changes as the k_{HI} modes switches to another candidate. In both these cases this mode continues to become more unstable as h is decreased. While as we increase the boundary layer thickness h these modes move into the usual modal sum while being stable. When potentially two k_{HI} modes are present, it has been in all cases observed that only one is found to be an instability or to have been stabilised by the branch cut, while the other mode behaves as a standard cut-off mode. We will later observe that, when varying the impedance Z, the two modes are inter-related.

III.A.2. The critical boundary layer thickness for stability

From the results shown here, since only one mode has been found to be a hydrodynamic instability in each case, unless it has been stabilised by the critical layer, it can be inferred that the hydrodynamic instability is stabilized by the critical layer branch cut provided the boundary layer is sufficiently thick. In what follows, we define a critical boundary layer thickness h_c for which the k_{HI} mode is located exactly on the critical layer branch cut. As such, the k_{HI} mode is stable for $h > h_c$, and is unstable for $h < h_c$. We calculate h_c here numerically by tracking the location of the k_{HI} mode as the boundary layer thickness is varied, seeking smaller imaginary parts until a real value is achieved; this is greatly aided by using the Frobenius solution method of Ref. 25 which allows tracking modes behind the critical layer branch cut.

III.B. Variation of stability with other parameters

We now proceed to vary the Mach number, frequency and impedance. In each case, we interpret the results both in terms of the locations of modes in the k-plane, and in terms of the critical boundary layer thickness h_c that stabilizes the flow.

8
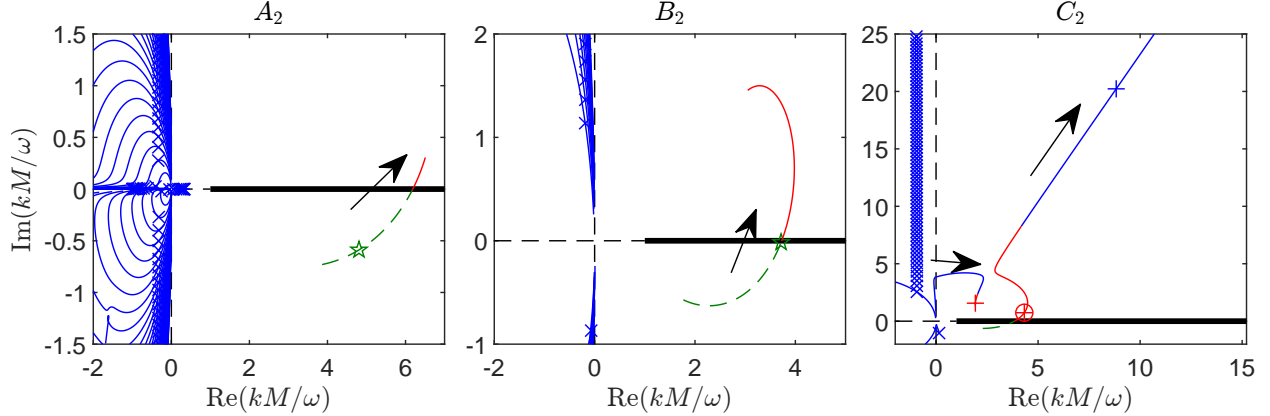
Fig. 5 Movement of the modal solutions in the complex k plane as the Mach number is varied from 0.1 to 0.9 in the direction of the arrows, for parameter sets A_2, B_2 and C_2 given in table 1. The axes have been scaled by M/ω in order to keep the location of the critical layer branch cut fixed. The location of the unstable k_{HI} mode for set C_1 has also been included and is circled.

III.B.1. Varying the mean flow Mach number

Figure 5 shows the results of varying the Mach number M. In order to keep the critical layer fixed as the Mach number is varied, note that a k-plane scaled by $M/\omega = 1/\text{St}$ is used, where St is the Strouhal number*. Figure 5 shows that, as the Mach number is decreased while keeping the boundary layer thickness constant, the flow is stabilised. At the same time, for lower flow speeds there are fewer cut-on modes, and as $M \to 0$ the modes approach their no-flow equivalents, as expected. When there are two candidate k_{HI} modes, again we find that only one of them may be unstable, and the other will be stabilised by moving into the usual modal sum, figure 5(C). It can be noted that in comparison to figure 4, for this parameter set the other potentially unstable mode experiences stabilisation by the critical layer. Since it has been observed that only one k_{HI} can be unstable or hidden behind the branch cut, it is important to observe that if we were to vary the Mach number and boundary layer thickness together, the same modes and stability would be found for any particular pair. The same further holds true for each of the other parameters. As a result, h_c appears to be continuous. When finding the value of h_c it is in many cases easier to find the value for a given parameter set and continuously vary the other parameters to a different case without having to locate the modes for a given boundary layer thickness first.

Figure 6 shows how h_c and $k_{\text{HI}}(h_c)$ vary as the Mach number is varied. Note that, by definition, $k_{\text{HI}}(h_c)$ is real and located on the critical layer branch cut. As expected from figure 5, we observe that h_c increases as the Mach number is increased. This appears to follow a remarkably linear trend, with a gradient depending on the other parameters. We note, however, that numerically it becomes increasingly difficult to track the value of h_c for small Mach numbers, as k_{HI} becomes increasingly large for small M. Considering the application to aircraft engines it is worth while considering that the Mach number will vary throughout the flight; thus, for the same liner, it could be expected that different stability is observed in the model between take off, in flight, and landing.

III.B.2. Varying the frequency

In a similar way to varying the Mach number, we may vary the frequency ω, as shown in figures 7 and 8. Once again we have scaled the complex k plane in figure 7 by $\frac{M}{\omega}$ in order to keep the critical layer branch cut fixed. It can be observed that a hydrodynamic instability may be present only for a range of intermediate frequencies (B_2) and (C_2), with both high and low frequencies being stable for thinner boundary layer thicknesses, while for sufficiently thick boundary layers (not included here) stability is found at all frequencies. This could be of particular importance for time domain simulations, where all resolved frequencies are present and consequently where instabilities cannot be avoided numerically by restricting the frequency range of interest. It can additionally be noted that when two potential k_{HI} modes are present, which one that stabilises through the critical layer changes as we approach the high and low frequency range (C_2).

---

*In dimensional terms, the rescaled axial wavenumber $kM/\omega = U(0)/(\omega/k)$, which is the ratio of the mean flow velocity to the perturbation phase velocity, and does not depend on the sound speed c_0 or the duct radius a.
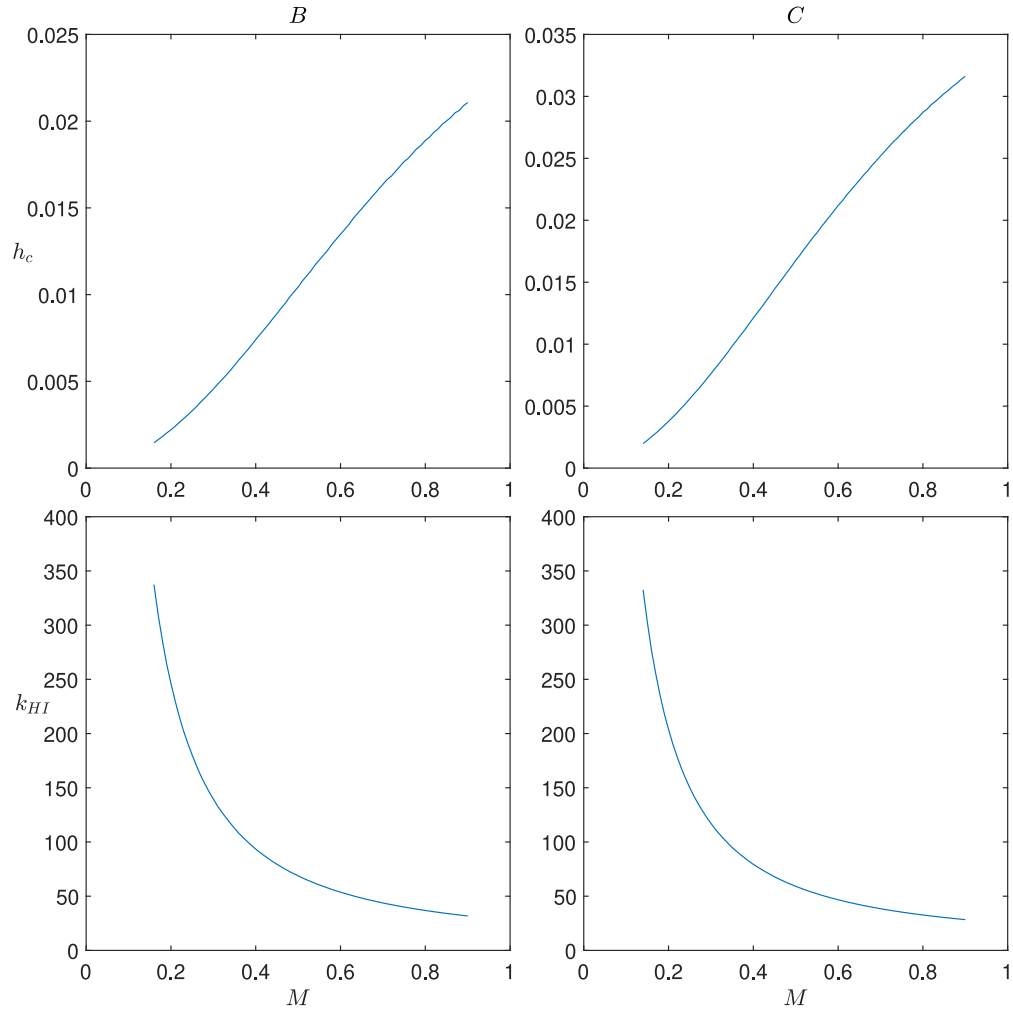
Fig. 6 (Top) Value of h_c plotted as the Mach number is varied. (Bottom) Value of $k_{HI}(h_c)$ for the hydrodynamic instability as the Mach number is varied.
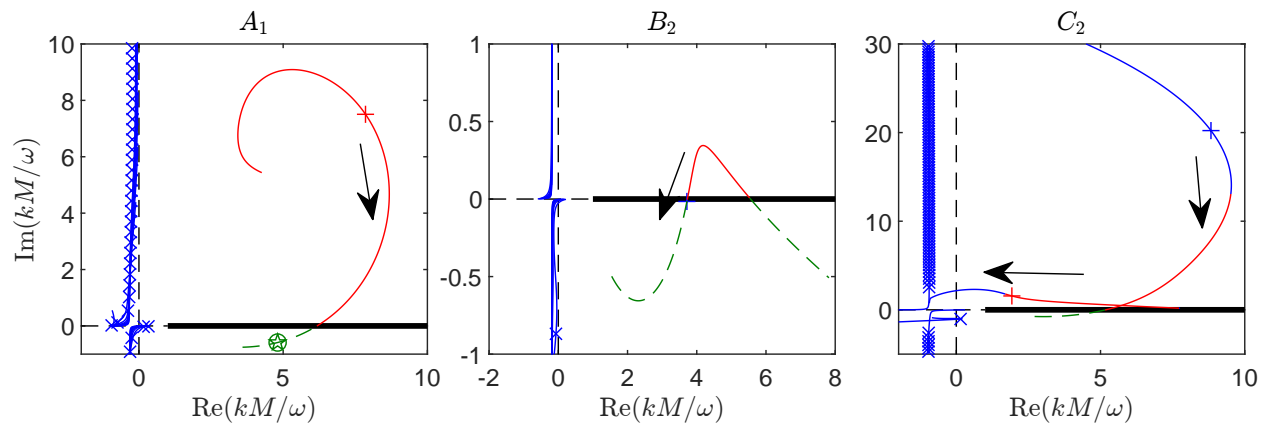
Fig. 7 As for figure 5, but for varying frequency ω from 1 to 50 in the direction of the arrows. Note that $Z(\omega)$ varies as ω is varied. Plotted are parameter sets A, B_2 and C_2. The k_{HI} mode of set A_2 has also been included, and is circled.
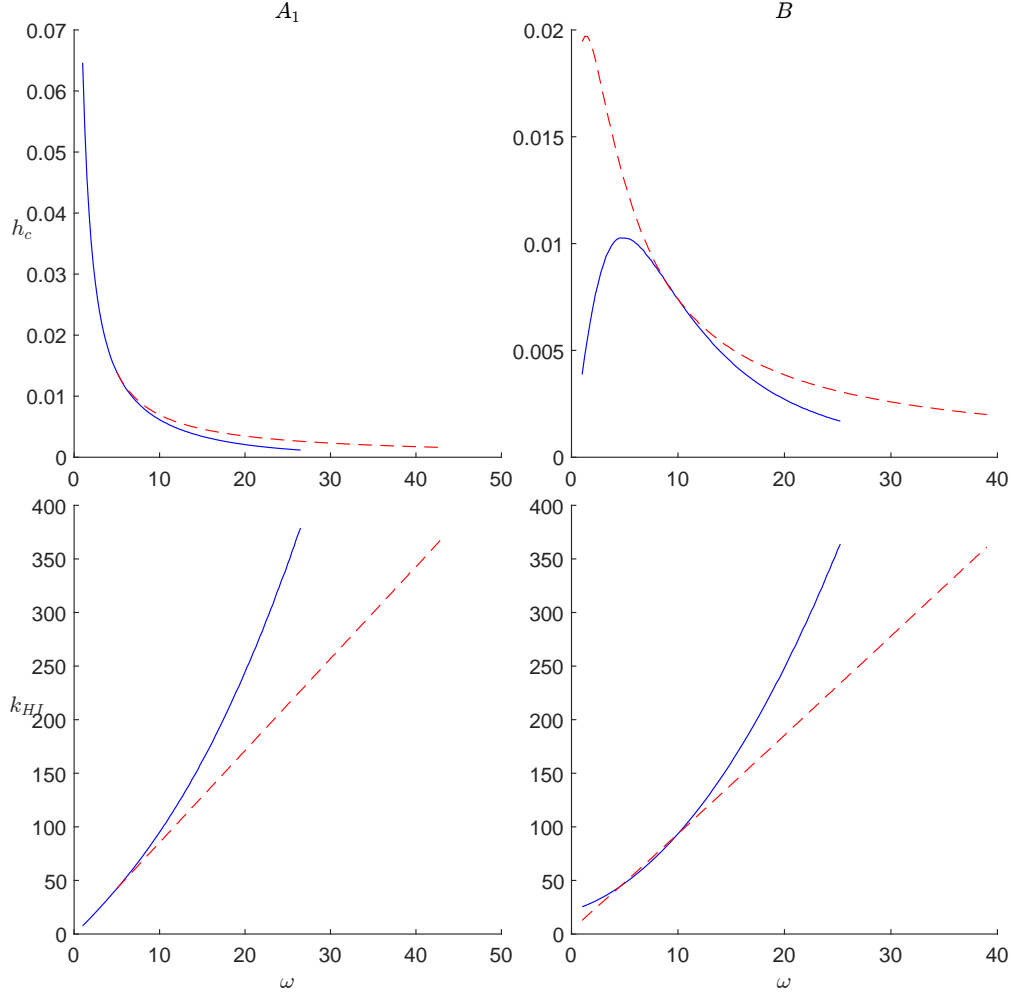
Fig. 8 As figure 6, but for varying the frequency. **(Blue) considering** $Z = Z(\omega)$**; and (red)** Z **fixed as given in table** 1**. Plotted are sets** A_1 **and** B**.**

It is worth observing that since we are making use of the Mass-Spring-Damper model for the impedance, the impedance also varies with frequency, and so it is not immediately clear if the stability being observed is due to the variation of the frequency, or due to the wall becoming harder in both high and low frequency limits. Because of this, in figure 8 the values of h_c and k_{HI} are additionally plotted for a fixed (and therefore unphysical) impedance, with the value as given in table 1. It may be observed that stabilisation is still observed for both low and high frequencies even in the fixed frequency case. We therefore hypothesise that the stability is caused by the frequency directly and not by the varying impedance. We note in passing that $k_{\mathrm{HI}}(h_c)$ appears to follow a linear relationship for the fixed wall impedance, although we do not investigate this further here.

III.B.3. Varying the lining impedance

Figures 9 and 10 show the effect of varying the impedance Z for fixed frequency ω. In figure 9 we only track the location of the modes as the reactance, $\mathrm{Im}(Z)$, is varied. While figure 10 gives a contour plot of the variation of h_c and $k_{\mathrm{HI}}(h_c)$ as both real and imaginary parts of Z, the resistance and reactance, are both varied. This contour plot is limited for large $|Z|$ due to numerical accuracy, as once again the value of $k_{\mathrm{HI}}(h_c)$ becomes too large. However, we may still conclude that, as $|Z| \to \infty$ and the duct becomes hard walled, the flow is stable for any finite thickness boundary layer. This is observed in figure 9 by looking at the modal location in both hard wall limits, $\mathrm{Im}(Z) \to \pm\infty$, indicated with a triangle, and in figure 10 by observing that h_c is decreasing as $|Z|$ becomes larger. We comment on this further in section III.C, as it contrasts with the unstable behaviour predicted for hard walls with other flow profiles.
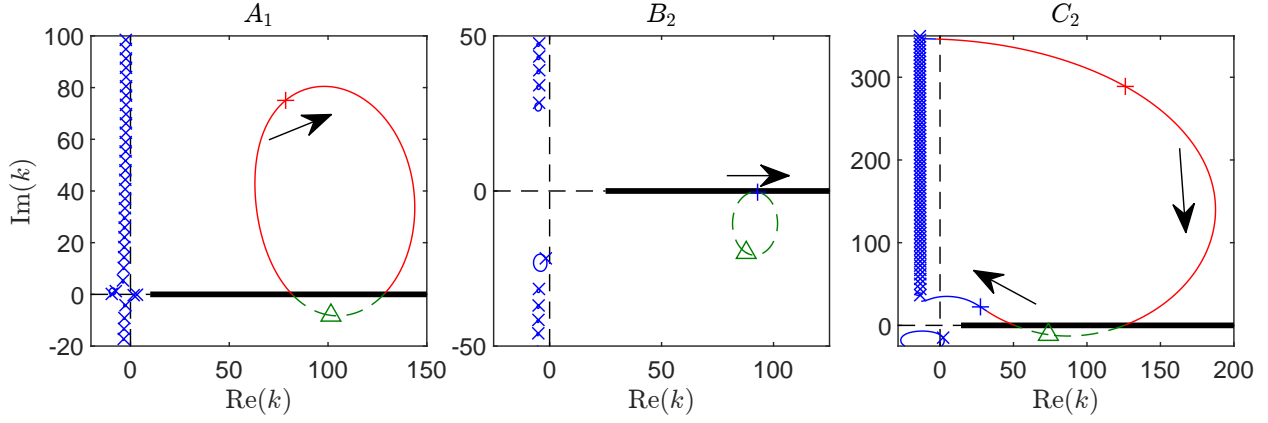
Fig. 9 Locations of the modal solutions in the complex k-plane as the reactance, $\mathrm{Im}(Z)$, is varied from $-\infty$ to ∞ in the direction of the arrows. The hydrodynamic instability for $|Z| = \infty$ is indicated by a triangle ($\triangle$). Plotted are sets A_1, B_2 and C_2.
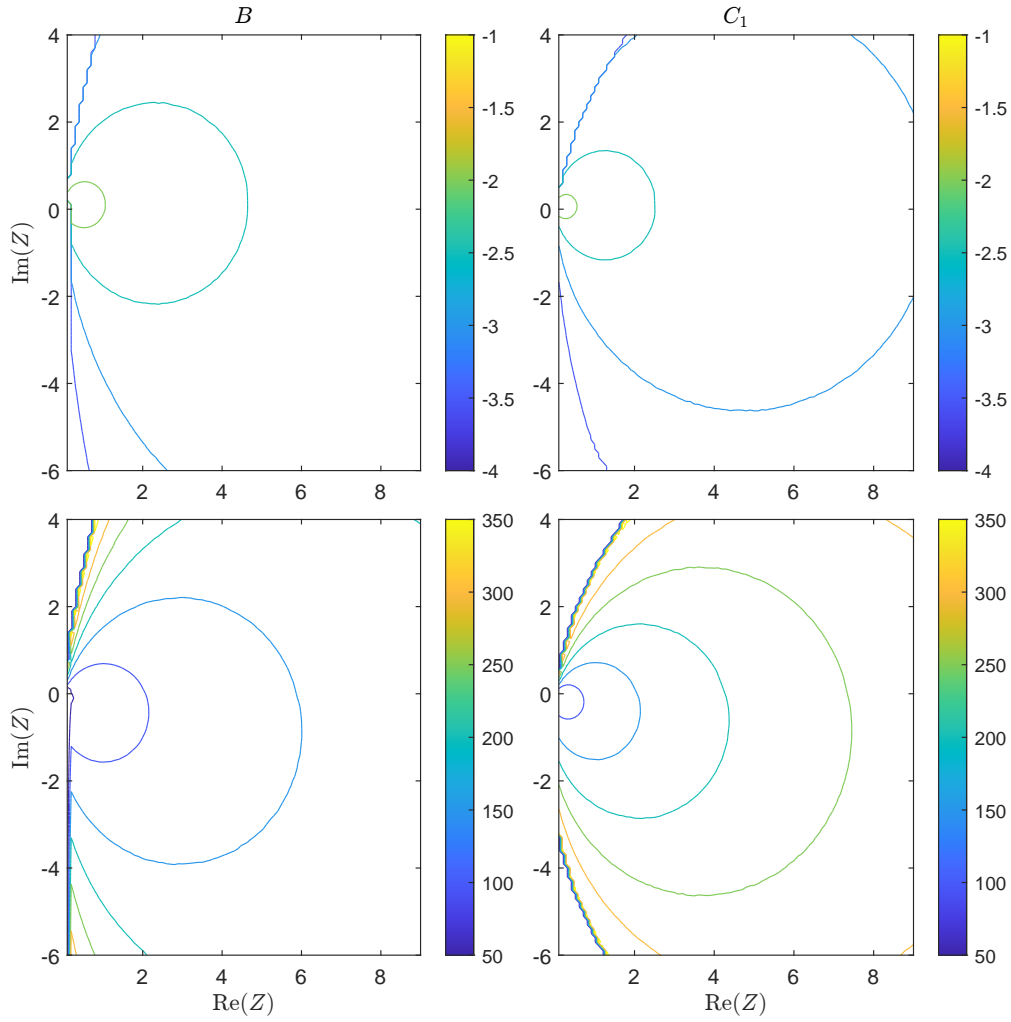
Fig. 10 Contour plot of h_c (top) and $k(h_c)$ (bottom) against $\mathrm{Re}(Z)$ and $\mathrm{Im}(Z)$. Values of h_c are indicated on a $\log_{10}$ scale. The large wrinkled outer circle denotes the limits of numerical resolution.

12

In figure 9 it can be seen that stability occurs for both large positive and negative reactance, $|\text{Im}(Z)| \to \infty$; in fact, this is also what happens as $\text{Re}(Z) \to \infty$, or indeed as $|Z| \to \infty$ with any passive impedance $\text{Re}(Z) \geq 0$. In all these cases, the same modes in the complex k-plane are recovered, corresponding to a hard wall $Z = \infty$, all of which are stable. Therefore, there are no unstable modes provided the wall is sufficiently hard; this is unlike for the Ingard–Myers boundary condition, as discussed below and plotted in figure 18. Indeed, in some cases (B_2), stability is observed for all impedances.

In order to investigate the dependence on frequency and impedance further, figure 11 illustrates the value of h_c as the impedance mass, spring and damping terms are varied. From these graphs two different behaviours may be observed. Firstly, when varying either the impedance mass or spring coefficient, if we choose to maintain a constant impedance, as indicated in figure 11 by the dashed lines, as we increase the frequency we do indeed observe a stabilising effect; that is, as ω is increased, h_c decreases. However we appear to observe a destabilization as the frequency is decreased at fixed impedance, although as seen in figure 8, this may be stabilising again for suitably small frequencies. A second observation is that, when the damping coefficient is small (as in C_1), it is found that the impedances with the largest h_c are those close to the resonant liner frequency $\omega = \sqrt{K/\mu}$ which gives $\text{Im}(Z) = 0$. This is shown most clearly in the right column of figure 11, but is also seen in the bottom left of figure 11 near $R = 0$. Moreover, as the damping coefficient increases the frequency with the largest value of h_c appears to reduce to zero.

III.C. Comparison to other flow profiles

The Frobenius solution used here to track the modal locations is specific to a quadratic shear flow profile. However, a similar Frobenius expansion exists for a linear flow profile [18], and an infinitely-thin boundary layer of arbitrary profile may be modelled using the Ingard–Myers boundary condition [7], such as was used to initially discover the hydrodynamic instability [4]. We may therefore repeat the analysis above to compare these boundary layer profiles, and a significant difference is seen.

III.C.1. Comparison with a linear flow boundary layer

Figures 12-15 show comparable results to those given above for the boundary layer thickness, Mach number, frequency, and impedance, but for a linear rather than quadratic boundary layer flow profile. In each of these it can be observed that the linear flow profile is unstable for all boundary layer thicknesses, and so no equivalent of h_c exists, and the hydrodynamic instability will always be present. There is some similarity, however, and for cases where stability was found for the quadratic shear, in the linear case we instead have a hydrodynamic instability with a small imaginary part. As a result of this, the growth rate of the mode remains exponential in the linear case, albeit with a small exponent, and thus it will still dominate eventually in the far-field, though it may be comparable in size within the near field. In addition, for the linear flow profile we also find an additional stable mode located below the branch cut (and not behind the branch cut), that may move above and behind the branch cut as the parameters are varied, although this mode would then stop contributing instead of becoming unstable. This mode, when it is located below the branch cut, has a contribution that is exactly cancelled by part of the contribution from the critical layer branch cut, and so in all cases it does not contribute to the final Fourier inversion. For this reason it has not been included in our mode plots for the linear shear flow.

III.C.2. Comparison with an infinitely-thin flow boundary layer

For comparison, also given here are the modal locations for a uniform flow profile using the Ingard–Myers boundary condition as parameters are varied, shown in figures 16–18, except that there is no variation of boundary layer thickness as no equivalent parameter exists. It is worth while observing that the critical layer branch cut also has no equivalent for the uniform flow case. Instead of requiring a Frobenius Series solution in this case, the solutions are given fully by Bessel functions, although subjected to a different boundary condition at $r = 1$.

When tracking the mode locations for the uniform flow profile under the Ingard–Myers boundary condition, for the Mach number we observe a stabilising effect from decreasing the Mach number, with the k_{HI} mode joining the usual modal sum, although unlike where this occurs in the sheared flow cases, for example figures 5(C) and 13(C), where there is still a different k_{HI} mode, in this case the behaviour just changes. This change of stability is therefore indicative the problem being ill-posed, i.e. we can not perform the Briggs-Bers Criterion. More information on the ill-posedness can be found in [8]. This same difficulty is additionally found when the frequency and impedance are varied. When varying the impedance it can be observed that we do once again find a stable flow profile for hard walled ducts, although
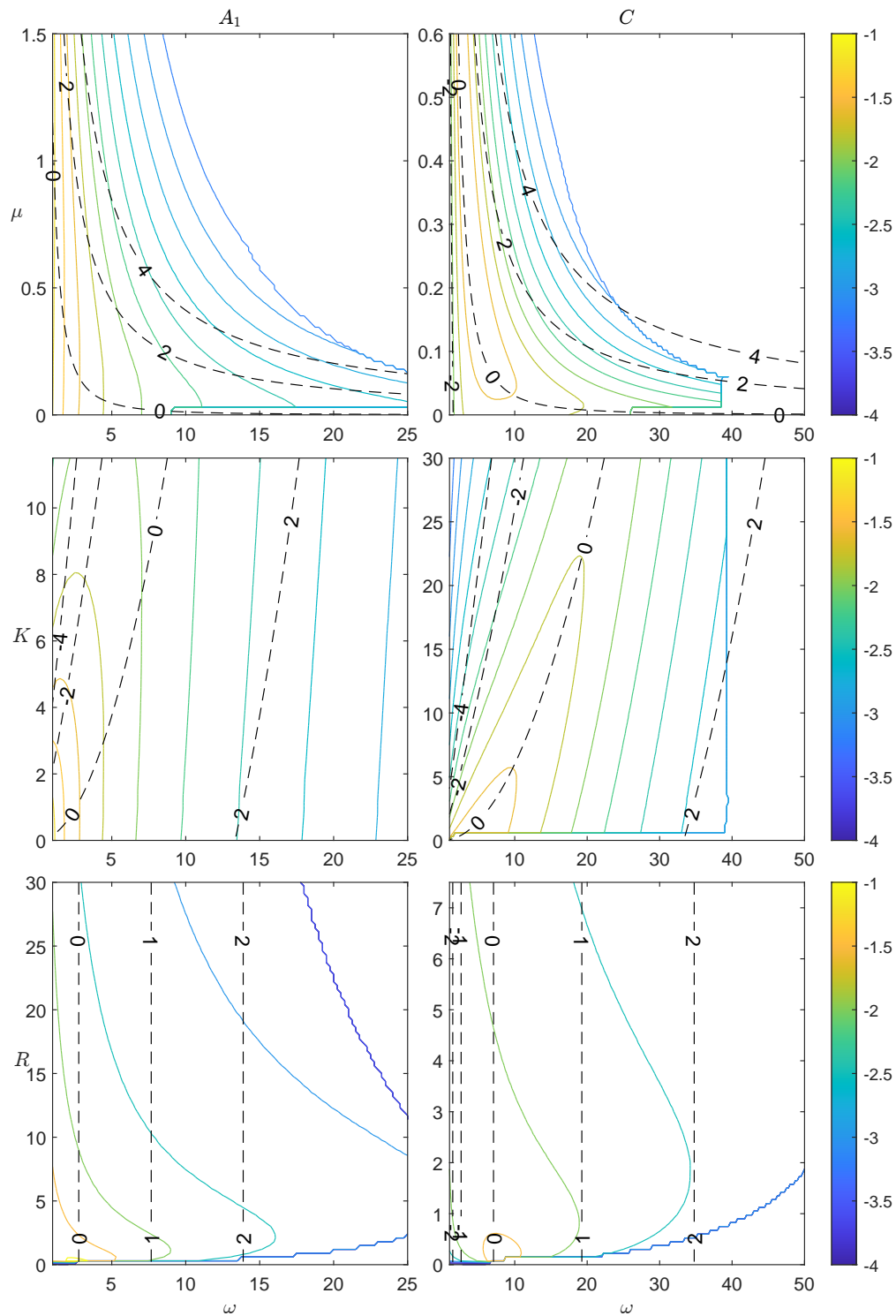
Fig. 11 Contour plots of h_c (on a $\log_{10}$ scale) as the frequency and impedance are varied, performed for Parameter Set A_1 and C_1, with the impedance mass μ, spring K and damper R terms being varied between 0 and 10 times their original value. Black dashed lines ($--$) indicate lines of constant impedance $Z = Z(\omega)$ with the value of $\mathrm{Im}(Z)$ indicated.
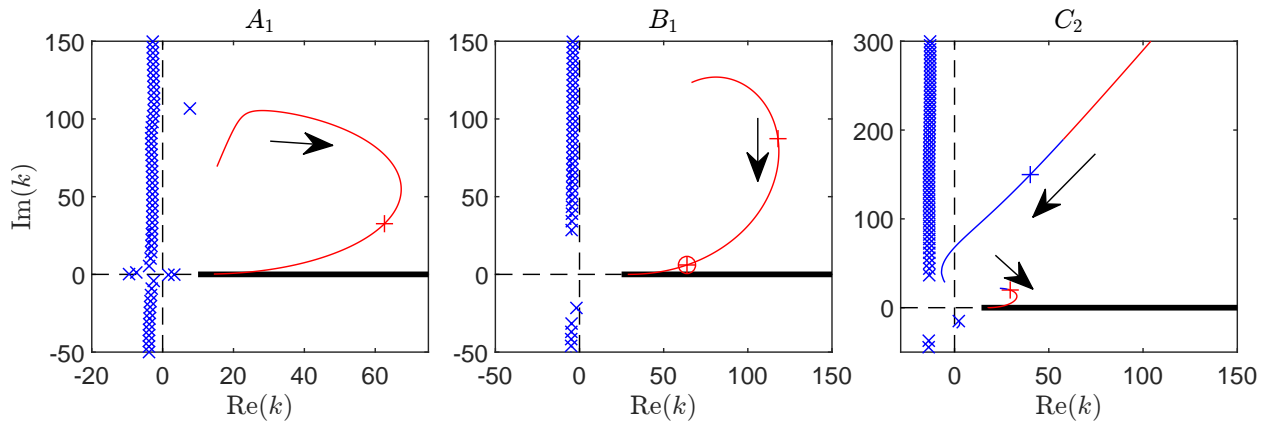
Fig. 12   As figure 4 varying boundary layer thickness h, for a linear shear flow profile.
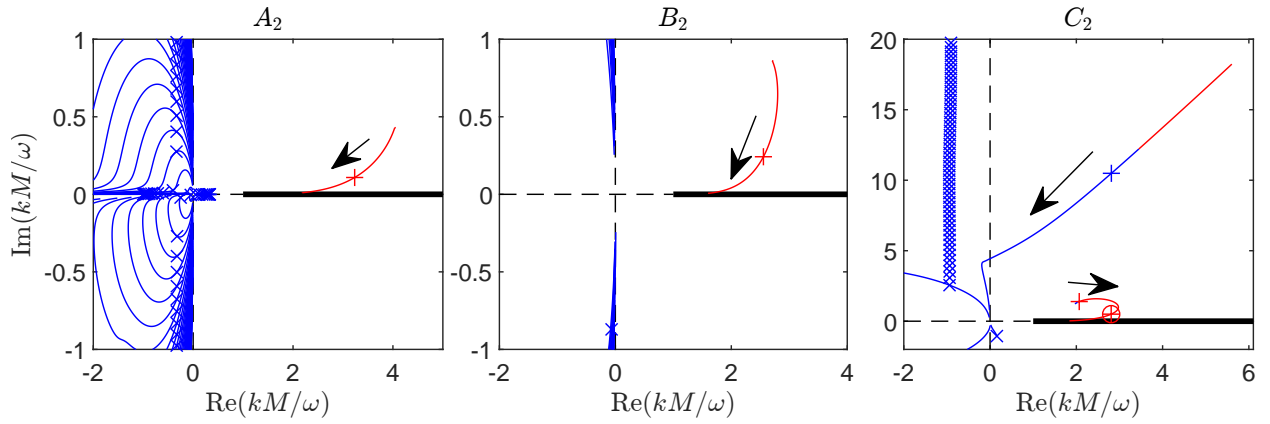
Fig. 13   As figure 5 varying the Mach number M, for a linear shear flow profile.
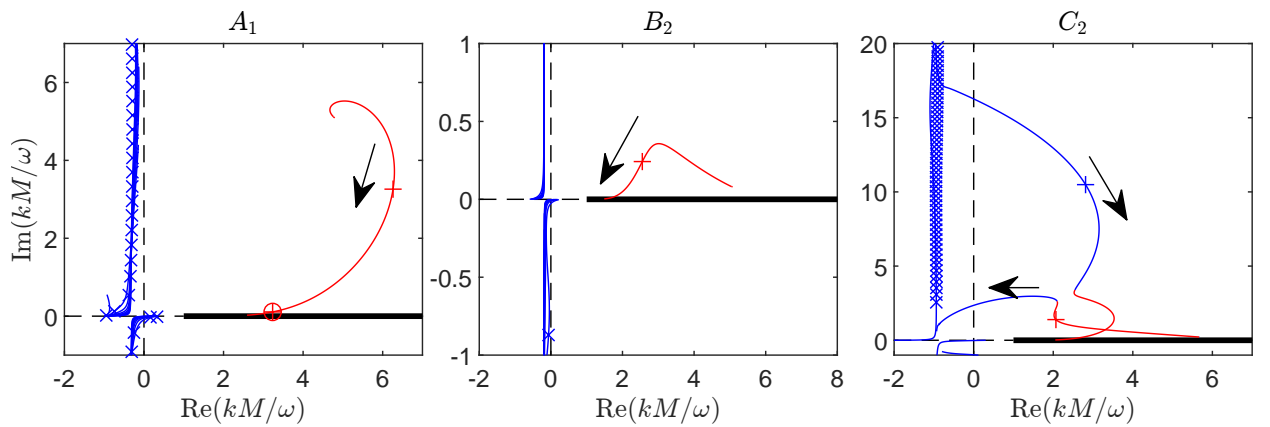
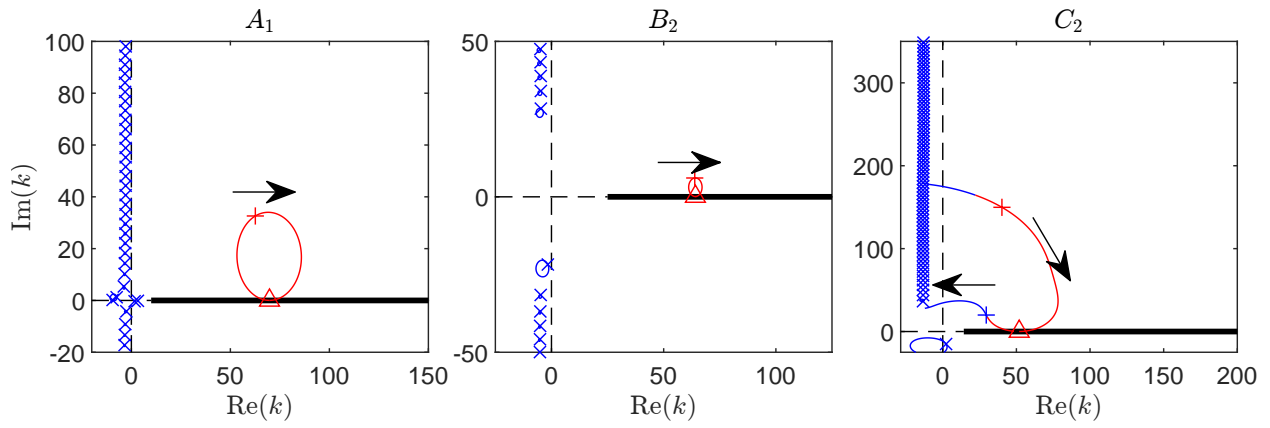**Fig. 14   As figure 7, varying the frequency ω, for a linear shear flow profile.**

15

Fig. 15 As figure 9, varying the impedance, $\mathrm{Im}(Z)$, for a linear shear flow profile.
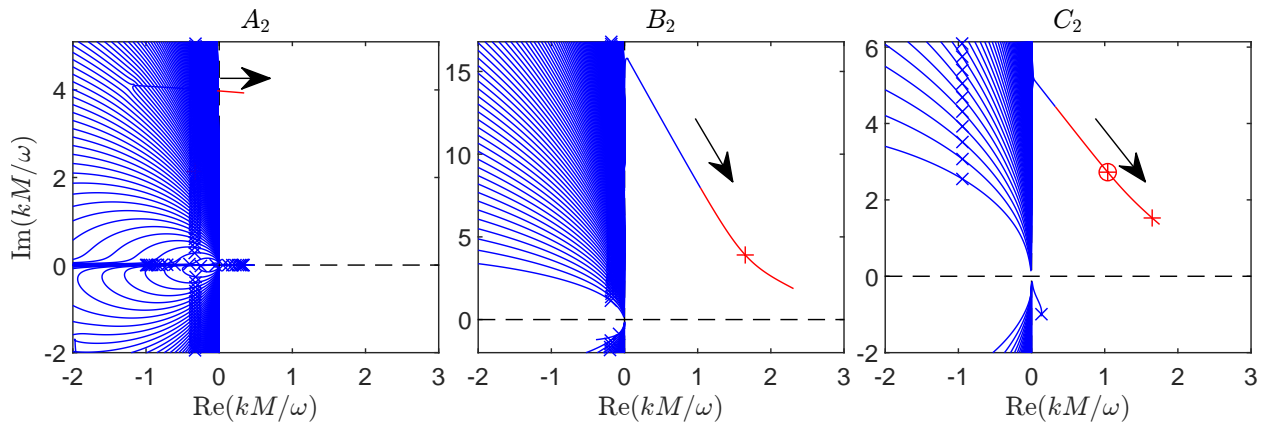

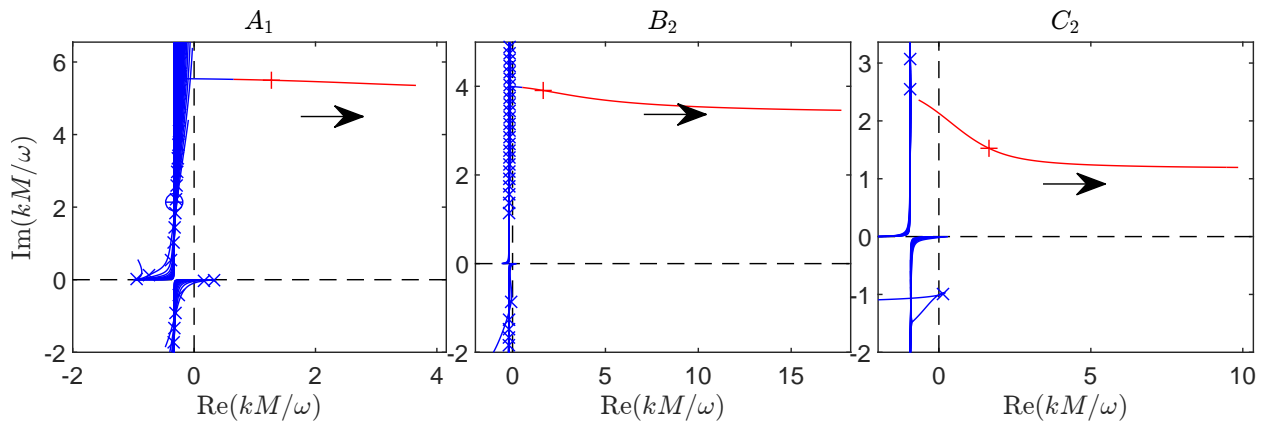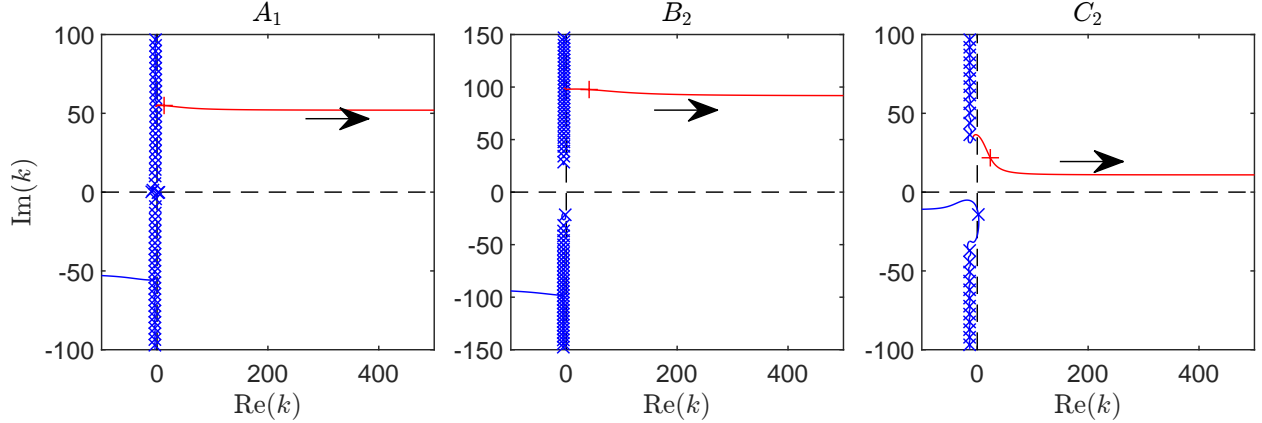**Fig. 16** As figure 5 varying the Mach number M, for a Uniform flow profile.

Fig. 17 As figure 7 varying the frequency ω, for a Uniform flow profile.

Fig. 18   As figure 9 varying the impedance, $\text{Im}(Z)$, for a Uniform flow profile.

the exact process of this varies depending on how we vary the impedance Z. As $\text{Im}(Z) \to +\infty$ we observe k_{HI} to have increasing real part, and for $Z = \infty$ the mode is not present. However, it remains true that for any large but finite impedance k_{HI} remains unstable and will continue to dominate the far-field, even if the small contribution and growth rate result in a negligible effect in the near field. This is unlike what is observed for the quadratic shear flow case, where a finite wall impedance will lead to stability, and the linear shear flow case where we always have unstable behaviour. Alternatively, as $\text{Im}(Z) \to -\infty$ the k_{HI} mode instead regains it's stability by moving into the usual acoustic modes, once again suggesting an ill-posedness of the problem.

This same behaviour is retrieved when varying the frequency, due to the relationship between the frequency and impedance through the mass–spring–damper model used. In both figures 17 and 18, $\text{Im}(k_{\text{HI}})$ appears to asymptote to a positive constant, although owing to the rescaled k-plane in figure 17, this is actually $\text{Im}(k_{\text{HI}})$ growing linearly in ω.

III.D. Modes shapes of the hydrodynamic instability.

Finally, we illustrate the mode shapes of the k_{HI} modes, both when it is a hydrodynamic instability and when it has been stabilised by the critical layer branch cut. These are given both as the variation in radius r at a particular axial location x (figure 19,) and as contour plots in the (x, r) plane (figure 20). In both the cases when the k_{HI} mode is unstable or stable, it is seen to be localized close to the duct wall, justifying its description as a surface wave mode. Additionally, it can be seen that when the mode is stable but with a small imaginary part (such as for parameter set B_2), the resulting mode shape is nearly cut-on and slowly-decaying in x.

Finally, by way of comparison, figure 21 shows the equivalent of the mode shape for the remainder of the (non-modal) contribution from the critical layer branch cut taken from Ref. 25, labelled $I(r, x)$ owing to its contribution as an integral, caused by a point source located either within the sheared flow and within the uniform flow. The critical layer has multiple contributing terms which decay algebraically in x, except when the source is located in the sheared flow, where a neutrally stable (non-decaying) term is also present. Further details can be found in Ref. 25. It can additionally be observed that the critical layer branch cut has a contribution that, while remaining near the wall, bleeds significantly further into the uniform flow region than the k_{HI} modes.

IV. Conclusions

We have considered a cylindrical duct with a parallel mean flow that has a boundary layer that varies quadratically near the wall; we note again that this boundary layer need not be thin. The MATLAB code from Ref. 25 was used to solve for the modes using a Frobenius solution method, allowing the modes to be tracked through the critical layer branch cut. It was shown in Ref. 25 that modes behind the critical layer branch cut no longer appear in the modal sum, but still contribute to the overall solution through the Fourier inversion integral around the critical layer branch cut; this can lead to the critical layer being the dominant contribution in the far-field downstream of a source, particularly when the source is located near the wall of the duct. Here, it is observed that the hydrodynamic instability surface mode k_{HI}
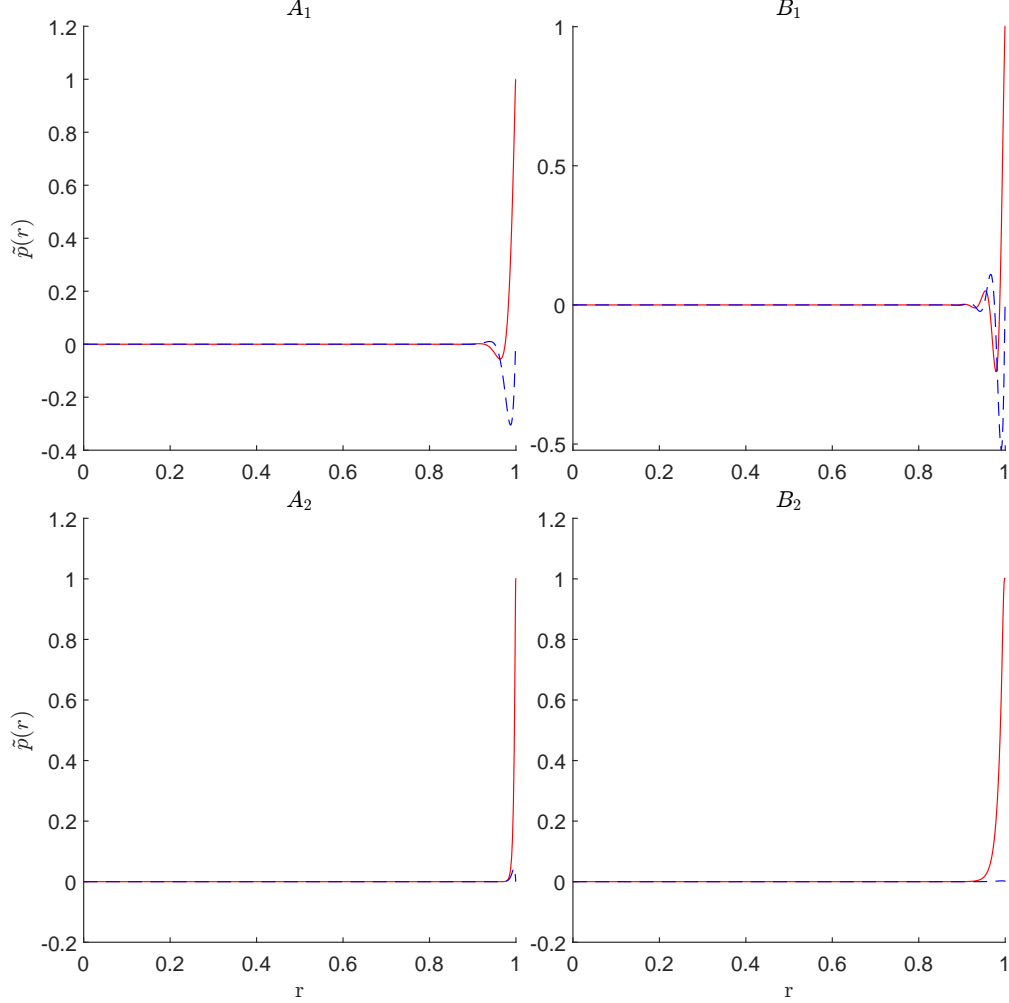
Fig. 19 **Pressure mode shapes $\widetilde{p}(r)$ for the unstable (A_1), (B_1) and stable (A_2), (B_2) k_{HI} modes, normalized such that $\widetilde{p}(1) = 1$.**

can be stabilized by its interaction with the critical layer. While it has previously been observed [22, 30] that increasing the boundary layer thickness has a stabilizing effect on absolute instabilities, here we further find that increasing the boundary layer thickness can completely stabilize the flow by effectively removing the instability mode by hiding it behind the critical layer branch cut. From this work, it would seem that the flow is always stable as $h \to 1$ irrespective of the impedance, flow speed, and frequency, implying that a purely parabolic Poiseuille flow is always stable; however, this is at present only a well-evidenced conjecture without a formal proof.

The exact boundary layer thickness h_c required for the stability varies depending on the Mach number, the frequency, and the impedance (figures 6, 8 and 10). When varying the centre-line Mach number, lower Mach numbers lead to less instability, manifesting as a smaller value of h_c. When varying the frequency, high- and low-frequencies are more stable, with often the hydrodynamic instability only being unstable for an intermediate range of frequencies around the resonant liner frequency of the boundary; this is true both when accounting for and when ignoring the frequency dependence of the impedance boundary. For a sufficiently thick boundary layer (depending on the parameters), the situation may be stable for all frequencies, which is an advantage of parabolic boundary layers that may be helpful for time-domain simulations compared with using either linear boundary layer profiles or infinitely-thin boundary layers, such as are implied by the Ingard–Myers boundary condition. When varying the impedance, the picture is more complicated (figure 11). As the impedance tends to a hard wall, $|Z| \to \infty$, we observe that h_c decreases, leading to less instability, and suggesting that as $|Z| \to \infty$ we will find that $h_c \to 0$ and any boundary layer thickness over a hard wall is stable; while this is expected, it contrasts with the linear boundary layer profile [18] which remains unstable as
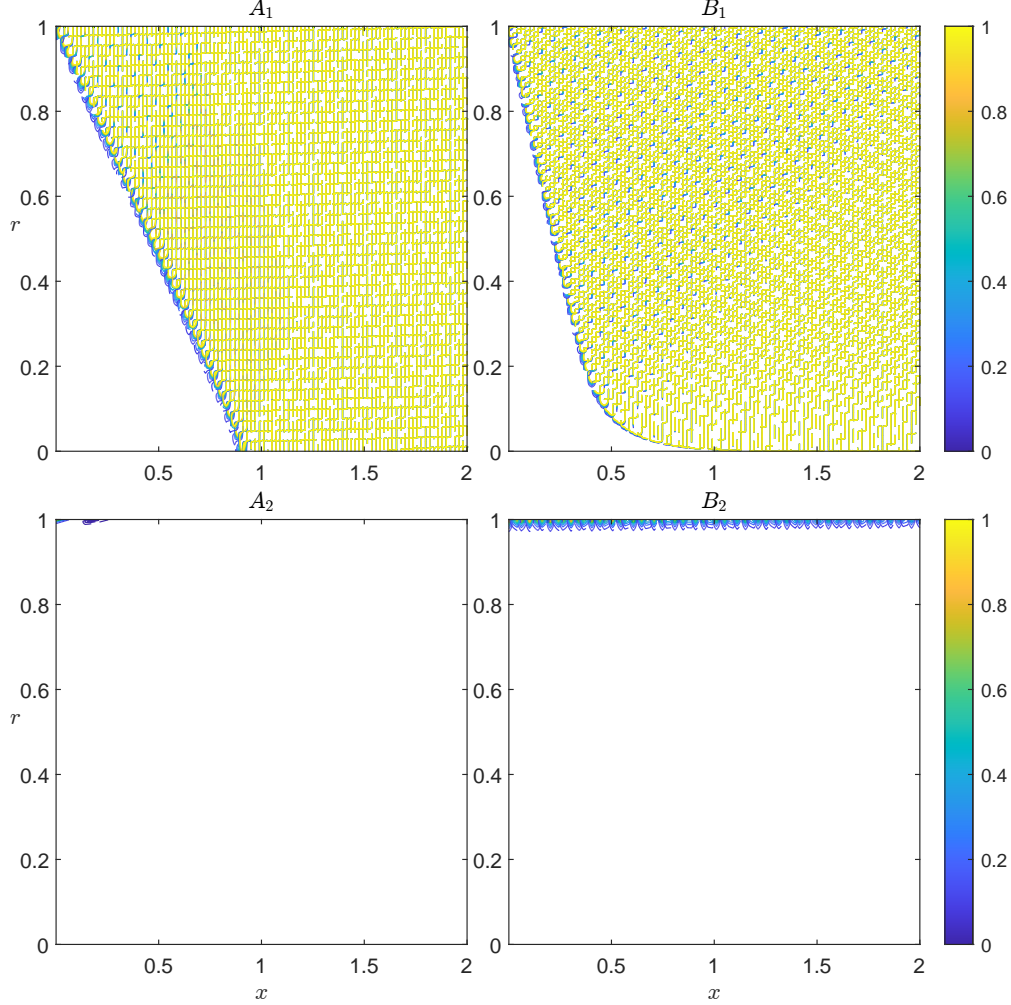
Fig. 20 **Pressure mode shapes** $Re(\widetilde{p}(r;k)e^{-\mathrm{i}kx})$ **in the** (x,r) **plane, for the** $k = k_{\mathrm{HI}}$ **modes.**

$|Z| \to \infty$. Additionally this is not the same stable behaviour observed for a uniform flow profile under the Ingard–Myers boundary condition, with stability found for larger but finite impedances in the quadratic shear flow case. However, it should be noted that numerical difficulty with the Frobenius algorithm is found when $|k|$ becomes too large, which limits the values of parameters that may be searched, particularly for very small Mach numbers or near-hard walls.

The stabilisation by the critical layer found here for a quadratic boundary layer profile is in contrast to the constant-then-linear flow profile of [18], for which the hydrodynamic instability seems to always be unstable. Stabilization by the critical layer has also been observed in the case of a tanh boundary layer profile, using a finite difference method to track the mode into the branch cut as the impedance was varied [39]. However, as this method could not analytically continue the solutions behind the branch cut, no further investigation could take place. We hypothesise this stabilisation behaviour will be typical of other smooth sheared flow profiles; indeed, it was acknowledged in [18] that the critical layer in the linear boundary layer profile case is rather artificial, and is caused by the cylindrical duct geometry rather than the sheared mean flow, unlike in the quadratic case. It is therefore possible that extending the modified-Myers boundary condition, or other such uniform flow impedance boundary conditions, to account for a quadratic shear flow profile may reveal important details for correctly predicting the location of the hydrodynamic instability, which has previously been the least well-predicted mode.

While this work has concentrated on the behaviours of the duct modes, we have not considered the amplitude with which these modes are excited by any given acoustic source, and how this compares to the nonmodal contribution from the branch cut itself. The same Frobenius technique [25] may be used to construct the Green's function for a point mass source, but how these various contributions would be excited by, for example, an incoming wave in a hard-walled duct
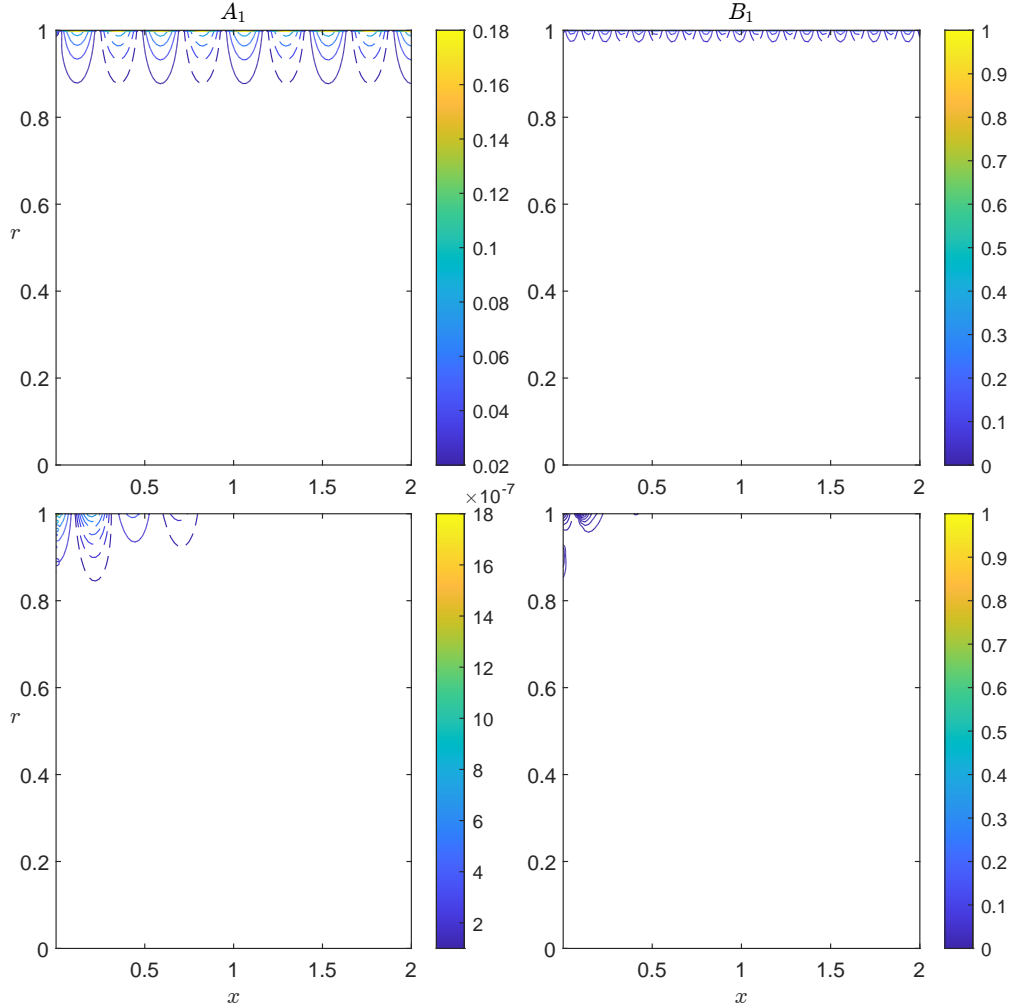
Fig. 21 Contour plot of the critical layer contribution $\mathrm{Re}(I(r,x))$ **in the** (x,r) **plane for a point mass source located in the sheared flow (top) and within the uniform flow (bottom). Note the different scales for contour values in each plot.**

scattering as it encounters a lined duct section, is still an open question [40, ch. 4]. Moreover, it would be interesting to investigate how the presence of the critical layer branch cut affects a Briggs–Bers stability analysis of absolute instability, and the corresponding critical boundary layer thickness needed for an absolute instability to be present, as was analysed without considering the critical layer branch cut in the 2D incompressible case [30] and the 3D compressible case in a cylindrical duct [10]. In particular, it would be theoretically possible that the hydrodynamic instability mode, even when it is behind the branch cut and is therefore stable, might still be able to interact with another upstream-propagating mode to lead to an absolute instability, and it would be interesting from a theoretical point of view to see whether this absolute instability could itself be behind the critical layer branch cut. These topics are left for future research.

Acknowledgments

References

[1] King, M. J., and Brambley, E. J., "Stabilisation of the Hydrodynamic Instability by the Critical Layer," AIAA paper, 2022-3096, 2022. doi:10.2514/6.2022-3096.

[2] Guess, A. W., "Calculation of Perforated Plate Liner Parameters from Specified Acoustic Resistance and Reactance," *J. Sound Vib.*, Vol. 40, No. 1, 1975, pp. 119–137. doi:10.1016/S0022-460X(75)80234-3.

[3] Tester, B. J., "The Propagation and Attenuation of sound in Lined Ducts containing Uniform or "Plug" Flow," *J. Sound Vib.*, Vol. 28, 1973, pp. 151–203. doi:10.1016/S0022-460X(73)80102-6.

[4] Rienstra, S., "A Classification of Duct Modes based on Surface Waves," *Wave Motion*, Vol. 37, 2003, pp. 119–135. doi:10.1016/S0165-2125(02)00052-5.

[5] Tam, C. K. W., and Auriault, L., "Time-Domain Impedance Boundary Conditions for Computational Aeroacoustics," *AIAA J.*, Vol. 34, No. 5, 1996, pp. 917–923. doi:10.2514/3.13168.

[6] Rienstra, S. W., "Impedance Models in Time Domain, including the Extended Helmholtz Resonator Model," AIAA paper 2006-2686, 2006. doi:10.2514/6.2006-2686.

[7] Myers, M., "On the acoustic boundary condition in the presence of flow," *J. Sound Vib.*, Vol. 71, No. 3, 1980, pp. 429–434. doi:10.1016/0022-460X(80)90424-1.

[8] Brambley, E., "Fundamental problems with the model of uniform flow over acoustic linings," *J. Sound Vib.*, Vol. 322, No. 4-5, 2009, pp. 1026–1037. doi:10.1016/j.jsv.2008.11.021.

[9] Renou, Y., and Aurégan, Y., "Failure of the Ingard–Myers Boundary Condition for a Lined Duct: An Experimental Investigation," *J. Acoust. Soc. Am.*, Vol. 130, 2011, pp. 52–60. doi:10.1121/1.3586789.

[10] Brambley, E., "A Well-posed boundary condition for acoustic liners in straight ducts with flow," *AIAA J.*, Vol. 49, No. 6, 2011, pp. 1272–1282. doi:10.2514/1.J050723.

[11] Gabard, G., "A comparison of impedance boundary conditions for flow acoustics," *J. Sound Vib.*, Vol. 332, No. 4, 2013, pp. 714–724. doi:10.1016/j.jsv.2012.10.014.

[12] Marx, D., and Aurégan, Y., "Effect of Turbulent Eddy Viscosity on the Unstable Surface Mode above an Acoustic Liner," *J. Sound Vib.*, Vol. 332, 2013, pp. 3803–3820. doi:10.1016/j.jsv.2013.02.005.

[13] Khamis, D., and Brambley, E., "Acoustics in a two-deck viscothermal boundary layer over an impedance surface," *AIAA J.*, Vol. 55, No. 10, 2017, pp. 3328–3345. doi:10.2514/1.J055598.

[14] Schulz, A., Weng, C., Bake, F., Enghardt, L., and Ronneberger, D., "Modeling of Liner Impedance with Grazing Shear Flow using a New Momentum Transfer Boundary Condition," AIAA paper, 2017-3377, 2017. doi:10.2514/6.2017-3377.

[15] Aurégan, Y., "On the use of a Stress–Impedance Model to describe Sound Propagation in a Lined Duct with Grazing Flow," *J. Acoust. Soc. Am.*, Vol. 143, No. 5, 2018, pp. 2975–2979. doi:10.1121/1.5037585.

[16] Weng, C., Schulz, A., Ronneberger, D., Enghardt, L., and Bake, F., "Flow and Viscous Effects on Impedance Eduction," *AIAA J.*, Vol. 56, No. 3, 2017, pp. 1118–1132. doi:10.2514/1.J055838.

[17] Spillere, A., Bonomo, L., Cordioli, J., and Brambley, E., "Experimentally Testing Impedance Boundary Conditions for Acoustic Liners with Flow: Beyond Upstream and Downstream," *J. Sound Vib.*, Vol. 489, 2020, p. 115676. doi:10.1016/j.jsv.2020.115676.

[18] Brambley, E., Darau, M., and Rienstra, S., "The critical layer in linear-shear boundary layers over acoustic linings," *J. Fluid Mech.*, Vol. 710, 2012, pp. 545–568. doi:10.1017/jfm.2012.376.

[19] Pridmore-Brown, D., "Sound propagation in a fluid flowing through an attenuating duct," *J. Fluid Mech.*, Vol. 4, No. 4, 1958, pp. 393–406. doi:10.1017/S0022112058000537.

[20] Gabard, G., and Astley, R., "A computational mode-matching approach for sound propagation in three-dimensional ducts with flow," *J. Sound Vib.*, Vol. 315, No. 4-5, 2008, pp. 1103–1124. doi:10.1016/j.jsv.2008.02.015.

[21] Yang, C., Fang, Y., Zhao, C., and Zhang, X., "On modeling the sound propagation through a lined duct with a modified ingard-myers boundary condition," *J. Sound Vib.*, Vol. 424, 2018, pp. 173–191. doi:10.1016/j.jsv.2018.03.022.

[22] Rienstra, S. W., "Acoustic scattering at a hard–soft lining transition in a flow duct," *Journal of Engineering Mathematics*, Vol. 59, No. 4, 2007, pp. 451–475. doi:10.1007/s10665-007-9193-z.

[23] Jiang, H., Hong Lau, A. S., and Huang, X., "An efficient algorithm of Wiener–Hopf method with graphics processing unit for duct acoustics," *Journal of Vibration and Acoustics*, Vol. 139, No. 5, 2017. doi:10.1115/1.4036471.

[24] Sobolev, A., and Yakovets, M., "Application of the Wiener–Hopf method for describing the propagation of sound in cylindrical and rectangular channels with an impedance jump in the presence of a flow," *Acoustical Physics*, Vol. 63, No. 6, 2017, pp. 625–636. doi:10.1134/S1063771017060148.

[25] King, M., Brambley, E., Liupekevicius, R., Radia, M., Lafourcade, P., and Shah, T., "The critical layer in quadratic flow boundary layers over acoustic linings," *J. Fluid Mech.*, Vol. 950, 2022, p. A8. doi:10.1017/jfm.2022.753.

[26] Swinbanks, M., "The sound field generated by a source distribution in a long duct carrying sheared flow," *J. Sound Vib.*, Vol. 40, No. 1, 1975, pp. 51–76. doi:10.1016/S0022-460X(75)80230-6.

[27] Briggs, R., "Criteria for Identifying Amplifying Waves and Absolute Instabilities," *Electron-Stream Interaction with Plasmas*, MIT, 1964, pp. 8–46. doi:10.7551/mitpress/2675.003.0004.

[28] Bers, A., "Space–time evolution of plasma instabilities — absolute and convective," *Basic plasma physics*, Vol. 1, edited by A. Galeev and R. Sudan, North-Holland, 1983, pp. 451–517.

[29] Brambley, E., "Surface modes in sheared boundary layers over impedance linings," *J. Sound Vib.*, Vol. 332, No. 16, 2013, pp. 3750–3767. doi:10.1016/j.jsv.2013.02.028.

[30] Rienstra, S. W., and Darau, M., "Boundary-layer thickness effects of the hydrodynamic instability along an impedance wall," *J. Fluid Mech.*, Vol. 671, 2011, pp. 559–573. doi:10.1017/S0022112010006051.

[31] Aurégan, Y., and Leroux, M., "Experimental Evidence of an Instability over an Impedance Wall in a Duct with Flow," *J. Sound Vib.*, Vol. 317, 2008, pp. 432–439. doi:10.1016/j.jsv.2008.04.020.

[32] Alomar, A., and Aurégan, Y., "Particle image velocimetry measurement of an instability wave over a porous wall in a duct with flow," *J. Sound Vib.*, Vol. 386, 2017, pp. 208–224. doi:j.jsv.2016.09.034.

[33] Marx, D., "Numerical Computation of a Lined Duct Instability Using the Linearized Euler Equations," *AIAA J.*, Vol. 53, No. 8, 2015, pp. 2379–2388. doi:10.2514/1.J053746.

[34] Deng, Y., Alomar, A., Dragna, D., and Galland, M.-A., "Characterization and Suppression of the Hydrodynamic Instability in the Time Domain for Acoustic Propagation in a Lined Flow Duct," *J. Sound Vib.*, Vol. 500, 2021, p. 115999. doi:10.1016/j.jsv.2021.115999.

[35] Dai, X., and Aurégan, Y., "A cavity-by-cavity description of the aeroacoustic instability over a liner with a grazing flow," *J. Fluid Mech.*, Vol. 852, 2018, pp. 126–145. doi:10.1017/jfm.2018.542.

[36] Bogey, C., Bailly, C., and Juvé, D., "Computation of Flow Noise using Source Terms in Linearized Euler's Equations," *AIAA J.*, Vol. 40, No. 2, 2002, pp. 235–243. doi:10.2514/2.1665.

[37] Ewert, R., and Schröder, W., "Acoustic Perturbation Equations based on Flow Decomposition via Source Filtering," *J. Comput. Phys.*, Vol. 188, No. 2, 2003, pp. 365–398. doi:10.1016/S0021-9991(03)00168-2.

[38] Richter, C., Lück, H., Panek, Ł., and Thiele, F., "Methods for Suppressing Shear Layer Instabilities for CAA," *J. Comput. Acoust.*, Vol. 19, No. 2, 2011, pp. 181–203. doi:10.1142/S0218396X11004420.

[39] Brambley, E. J., "Review of Acoustic Liner Models with Flow," *Proc. Acoustics 2012, Nantes, France*, 2012, pp. hal–00810687. URL http://hal.archives-ouvertes.fr/hal-00810687.

[40] King, M., "Mathematical Models of Aeroacoustics in Boundary Layers over Acoustic Linings," Ph.D. thesis, University of Warwick, 2023. WRAP 176897.